Linear-response time-dependent density functional theory approach to warm dense matter with adiabatic exchange-correlation kernels

Zhandos A. Moldabekov [1,2,*] Michele Pavanello,[3,4] Maximilian P. Böhme [1,2,5] Jan Vorberger,[2] and Tobias Dornheim[1,2]

[1]*Center for Advanced Systems Understanding (CASUS), D-02826 Görlitz, Germany*
[2]*Helmholtz-Zentrum Dresden-Rossendorf (HZDR), D-01328 Dresden, Germany*
[3]*Department of Chemistry, Rutgers University, 73 Warren St., Newark, New Jersey 07102, USA*
[4]*Department of Physics, Rutgers University, 101 Warren St., Newark, New Jersey 07102, USA*
[5]*Technische Universität Dresden, D-01062 Dresden, Germany*

We present a methodology for the linear-response time-dependent density functional theory (LR-TDDFT) calculation of the dynamic density response function of warm dense matter in the adiabatic approximation that can be used with any available exchange-correlation (XC) functional across Jacob's ladder and across temperature regimes. The uniqueness of the presented approach is that it can go beyond the adiabatic local density approximation and adiabatic generalized gradient approximation while preserving the self-consistency between the Kohn-Sham (KS) response function and adiabatic XC kernel for extended systems. The key ingredient to the presented method is the combination of the adiabatic XC kernel from the direct perturbation approach with the macroscopic dynamic KS response from the standard LR-TDDFT method using KS orbitals. We demonstrate the application of the method for the example of warm dense hydrogen, for which we perform a detailed analysis of the KS density response function, the random phase approximation result, the total density response function, and of the adiabatic XC kernel. The analysis is performed using local density approximation, generalized gradient approximation, and meta-generalized gradient approximation level approximations for the XC effects. The presented method is directly applicable to disordered systems such as liquid metals, warm dense matter, and dense plasmas.

I. INTRODUCTION

Warm dense matter (WDM) is relevant for a plethora of applications such as inertial confinement fusion (ICF) [1,2], laboratory astrophysics [3,4], and material science at extreme conditions [5–7]. WDM is generated in experiments, e.g., by laser heating or shock compression at facilities such as the National Ignition Facility [1,2,8], the European X-ray Free-Electron Laser [9], and the Linac coherent light source at SLAC [10]. In nature, WDM exists in the interior of white dwarfs [11,12] and giant planets [13,14], and in the outer layer of neutron stars [15]. Among various atomic composition possibilities, warm dense hydrogen is of particular importance. Indeed, hydrogen is the most abundant element in the universe and its isotopes are used as thermonuclear fuel in ICF applications. Recently, a breakthrough achievement on the path to ICF has been reported: a net positive energy outcome from fusion reactions compared to the energy used to start the fusion process has been detected. This makes the understanding of warm dense hydrogen and the development of reliable methods for WDM [16–18], in general, highly relevant.

At the extreme temperatures and densities realized in WDM experiments and within the aforementioned astrophysical objects, electrons are partially degenerate and strongly correlated. With regard to temperature and density, WDM occupies an intermediate region between solid states and dense plasmas. This is also reflected in the theoretical methods used for WDM research [18], some of which we discuss in this paper. Being a relatively new field compared to solid state physics and plasma physics, theoretical methods to describe WDM are still in the stage of active development. Among existing approaches, *ab initio* methods such as quantum Monte Carlo (QMC) [16,19–21] and thermal density functional theory (DFT) [18,22–24] are particularly important for a reliable description of experimental results and for providing guidance for new experimental developments.

One of the main theories for the description of many-particle systems is linear response theory (LRT). Although basic principles of LRT are general, LRT is formulated in somewhat different ways and with emphasis on different physical features in solid-state physics, in WDM studies, and in plasma physics. On the one hand, WDM is usually disordered and does not feature symmetries and well-defined crystal-structure-like solids. On the other hand, strong electron-ion and electron-electron correlations do not allow neglecting microscopic density inhomogeneities as is often the case for plasmas. Additionally, it is important for WDM to have access to the density response properties at wave numbers comparable or larger than the Fermi wave number since such wave

---

*z.moldabekov@hzdr.de

numbers are probed by the x-ray Thomson scattering (XRTS) technique [25,26], which is one of the main WDM diagnostic methods [27–30]. It is crucial to have a clear understanding of these aspects when tools developed for solids or plasmas are used for WDM studies.

An important example of such a tool is the linear-response time-dependent density functional theory (LR-TDDFT) approach. LR-TDDFT allows one to compute various electronic optical and transport properties [31]. The key quantity for the LR-TDDFT-based description is the density response function. Indeed, an accurate computation of the density response function is one of the main problems of WDM theory [18,32].

A quantity that is closely connected to the density response function is the exchange-correlation (XC) kernel, which can be defined as the functional derivative of the XC potential with respect to density [33]. The XC kernel is one of the key ingredients for the computation of the density response function using LR-TDDFT. Recently, Moldabekov *et al.* [34] presented an approach for the calculation of the static (adiabatic) XC kernel within KS-DFT for any available XC functional. This method is formulated for disordered systems that are homogeneous on average, e.g., WDM, dense plasmas, and liquid metals. This method is based on the direct perturbation of the system by a static harmonic potential [18,35–39]. The difference in the density between perturbed and unperturbed cases allows one to extract the static density response function. This static density response function is combined with a reference noninteracting density response function to compute the static XC kernel. The main utility of the static XC kernel within LR-TDDFT is the computation of the density response function. However, it had hitherto not been clear how to use the static XC kernel from the direct perturbation approach in the LR-TDDFT framework. Here, we formulate a consistent LR-TDDFT approach for disordered systems such as WDM that is based on the adiabatic (static) XC kernel obtained from the direct perturbation approach.

As the main result, we formulate a clear recipe for the computation of the linear density response function combining both the LR-TDDFT and direct perturbation method. Within this framework, LR-TDDFT is used to compute the macroscopic KS-response function taking into account the density inhomogeneity induced by ions (*local-field effects* [40,41]) and the direct perturbation method provides access to the static XC kernel for any XC functional. These two ingredients are combined to compute the macroscopic linear density response function of WDM. We apply this combined workflow to investigate density response properties and the XC kernel of warm dense hydrogen. We present a detailed numerical investigation of the density response function, the Kohn-Sham (KS) response function and its screened version in the random phase approximation (RPA), and of the XC kernel. To get insights into the role of XC effects, we use XC functionals on the level of the local density approximation (LDA), generalized gradient approximation (GGA) and meta-GGA. Although we mainly focus on WDM applications, the presented workflow is applicable for any disordered system that is homogeneous on average.

The paper is organized as follows: We begin with providing the theoretical background of LR-TDDFT, of LRT as used for homogeneous systems (such as plasmas), and of the direct perturbation approach in Sec. II; we conclude Sec. II by formulating an adiabatic approximation for the density response function based on the static XC kernel from the direct perturbation approach. The parameters and simulation details are given in Sec. III and we illustrate the application of the developed method for the example of warm dense hydrogen in Sec. IV. The paper is concluded by a summary of the main findings and a brief outlook on future applications.

II. THEORETICAL BACKGROUND

Different formulations and approaches are being used for the calculation and description of the linear density response function of electrons in WDM. First, there is the standard LR-TDDFT approach. It uses the KS density response function, which is based on KS orbitals, and the XC kernel [42]. In this case, the impact of ions on electrons is taken into account in both the KS response function and XC kernel through the density inhomogeneity induced by the ions (local-field effects). Another often-used approach, originally developed for dense plasma physics, is based on the ideal Lindhard response function and the so-called local field correction (LFC) [43], which incorporates everything else that is missing in the Lindhard function (not to be confused with local-field effects in the LR-TDDFT) [32,44–46]. This is not only a standard plasma physics approach but is also commonly used in the quantum theory of homogeneous electron liquid [43,47]. From a computational point of view, an alternative to the LR-TDDFT is to use a direct perturbation by an external field to measure the density response function connecting the perturbing field with the density change induced by it [48–50]. These different formulations and methods for a dynamic density response function have been actively used in WDM studies [39,51–54]. However, in many aspects, the connection between them has not been clearly formulated and understood.

The main goal of this paper is to formulate a consistent LR-TDDFT approach for WDM that is based on an adiabatic (static) XC kernel from the direct perturbation approach introduced in Ref. [34]. We will first discuss the dynamic dielectric function from LR-TDDFT, followed by an introduction to LRT as used in the physics of dense plasmas and the direct perturbation approach to the static XC kernel. This allows us to present a clear connection between these schemes and a recipe for LR-TDDFT calculations of the macroscopic density response of WDM with an adiabatic XC kernel on any rung of Jacob's ladder.

A. Dynamic dielectric function from LR-TDDFT

We start with a brief summary of what is needed from LR-TDDFT for further discussion of the connection between the latter and the direct perturbation approach.

The microscopic dynamic dielectric function, for momentum **k** and energy ω, is expressed in terms of the microscopic density response function as [42]

$$\varepsilon^{-1}_{\mathbf{G},\mathbf{G}'}(\mathbf{k}, \omega) = \delta_{\mathbf{G},\mathbf{G}'} + \frac{4\pi}{|\mathbf{k} + \mathbf{G}|^2} \chi_{\mathbf{G},\mathbf{G}'}(\mathbf{k}, \omega), \qquad (1)$$

where **k** is a wave vector restricted to the first Brillouin zone, and **G** and **G**$'$ are reciprocal lattice vectors.

The Fourier coefficients $\chi_{G,G'}(\mathbf{k}, \omega)$ of the density response matrix are computed using a Dyson's-type equation [55–57]:

$$\chi_{GG'}(\mathbf{k}, \omega) = \chi_{GG'}^0(\mathbf{k}, \omega) + \sum_{G_1 G_2} \chi_{GG_1}^0(\mathbf{k}, \omega) \big[v_{G_1}(\mathbf{k}) \delta_{G_1 G_2}$$
$$+ K_{G_1 G_2}^{xc}(\mathbf{k}, \omega) \big] \chi_{G_2 G'}(\mathbf{k}, \omega), \qquad (2)$$

where $\chi_{G,G'}^0(\mathbf{k}, \omega)$ is a noninteracting density response function, $v_{G_1}(\mathbf{k}) = 4\pi/|\mathbf{k} + \mathbf{G}_1|^2$ is the Coulomb potential, and $K_{G_1,G_2}^{xc}(\mathbf{k}, \omega)$ is the XC kernel. The noninteracting density response function $\chi_{G,G'}^0(\mathbf{k}, \omega)$ is computed using the KS orbitals and corresponding energy eigenvalues from a KS-DFT simulation of an equilibrium state [58].

There are numerous approximations for the XC kernel in Eq. (2), which we do not discuss in this paper (see, e.g., Refs. [55,59] for more information). We only note that the XC kernel is defined as the functional derivative of the XC potential with respect to density [42].

A commonly used approximation for the XC kernel that is considered in this paper is the adiabatic (static) approximation $K_{G_1,G_2}^{xc}(\mathbf{k}) = K_{G_1,G_2}^{xc}(\mathbf{k}, \omega = 0)$. For extended systems with sampling of the Brillouin zone, currently there is no possibility to compute $K_{G_1,G_2}^{xc}(\mathbf{k})$ using the functional derivative of the XC potential beyond the adiabatic LDA (ALDA) and GGA (AGGA) [55]. This is meant in the sense of the self-consistent calculation where the XC kernel is fully compatible with the XC functional used for the KS-DFT simulation of the equilibrium state.

The response of a system to an external monochromatic perturbation with wave vector $\mathbf{q} = \mathbf{k} + \mathbf{G}$, e.g., in the case of the XRTS diagnostics, is described by the value of the microscopic dynamic dielectric function Eq. (1) with $\mathbf{G} = \mathbf{G}'$:

$$\varepsilon_M(\mathbf{q}, \omega) = \frac{1}{1 + \frac{4\pi}{|\mathbf{q}|^2} \chi_{GG}(\mathbf{k}, \omega)}. \qquad (3)$$

We note that $\mathbf{q}$ in Eq. (3) is not restricted to the first Brillouin zone like $\mathbf{k}$. Additionally, we have $\mathbf{G} = \mathbf{G}' = 0$, if $\mathbf{q}$ is in the first Brillouin zone [57,60].

Further, following the LR-TDDFT terminology, we call the physical properties describing the response of a system to an external macroscopic perturbation as macroscopic; e.g., $\varepsilon_M(\mathbf{q}, \omega)$.

The RPA follows from setting $K_{G_1,G_2}^{xc}(\mathbf{k}, \omega) = 0$ in Eq. (2):

$$\chi_{GG'}^{RPA}(\mathbf{k}, \omega) = \chi_{GG'}^0(\mathbf{k}, \omega)$$
$$+ \sum_{G_1} \chi_{GG_1}^0(\mathbf{k}, \omega) \frac{4\pi}{|\mathbf{k} + \mathbf{G}_1|^2} \chi_{G_1 G'}^{RPA}(\mathbf{k}, \omega). \qquad (4)$$

Accordingly, the macroscopic dielectric function in the RPA reads

$$\varepsilon_M^{RPA}(\mathbf{q}, \omega) = \frac{1}{1 + \frac{4\pi}{|\mathbf{q}|^2} \chi_{GG}^{RPA}(\mathbf{k}, \omega)}. \qquad (5)$$

Next, we discuss the LRT formulation as used for homogeneous systems such as WDM and dense plasmas.

B. Linear density response theory in dense plasma physics

In LR-TDDFT, ions are considered to be an external field that affects electronic properties. In contrast, the LRT of plasmas is generally formulated taking into account both the response of ions and electrons to an external perturbation [61]. To be on the same level of description with the LR-TDDFT, we consider the response of electrons with fixed ions. We note that this is justified in situations where the perturbation time is much shorter than the reaction time of ions since the latter are much more inert compared to electrons [62].

The dielectric function of electrons in homogeneous systems is expressed using the density response function of electrons $\chi(\mathbf{q}, \omega)$ in the following form [47]:

$$\varepsilon^{-1}(\mathbf{q}, \omega) = 1 + v(q)\chi(\mathbf{q}, \omega), \qquad (6)$$

where $v(q) = 4\pi/q^2$.

It is a common practice in the quantum theory of the electron liquid and in dense plasma physics to express the density response function in terms of the ideal response function and the XC kernel [47,61,63],

$$\chi(\mathbf{q}, \omega) = \frac{\chi_0(\mathbf{q}, \omega)}{1 - [v(q) + K_{xc}(\mathbf{q}, \omega)]\chi_0(\mathbf{q}, \omega)}, \qquad (7)$$

where $\chi_0(\mathbf{q}, \omega)$ is a reference noninteracting density response function and the XC kernel is often defined using LFC:

$$K_{xc}(\mathbf{q}, \omega) = -v(q)G(\mathbf{q}, \omega). \qquad (8)$$

We note that in the case of the uniform electron gas (UEG), the XC kernel in Eq. (7) is the same as the XC kernel of the LR-TDDFT. However, in general, for disordered systems that can be considered homogeneous after averaging over different ionic configurations—such as WDM, dense plasmas, and liquid metals—a clear connection between the XC kernel in Eq. (7) and the microscopic XC kernel in the LR-TDDFT [e.g., in Eq. (2)] has not been provided.

The dielectric function in the RPA follows from setting $K_{xc}(\mathbf{q}, \omega) = 0$ in Eq. (7) and substituting the resulting $\chi(\mathbf{q}, \omega)$ into Eq. (6):

$$\varepsilon_{RPA}(\mathbf{q}, \omega) = 1 - v(q)\chi_0(\mathbf{q}, \omega). \qquad (9)$$

In plasma physics applications, it is common to use the Lindhard function (temperature-dependent version) as $\chi_0(\mathbf{q}, \omega)$ and approximate $G(\mathbf{q}, \omega)$ according to the free electron gas model [44,61].

For WDM applications, the correction due to electron-ion interactions to $\varepsilon(\mathbf{q}, \omega)$ is often included explicitly in the form of the electron-ion collision frequency in the so-called generalized Mermin model [25,44,64–66]. The relevant point is that this model is also based on the temperature-dependent Lindhard function and $G(\mathbf{q}, \omega)$. The Lindhard function for $\chi_0(\mathbf{q}, \omega)$ can be used when the composition of the system can be divided into well-defined species like free electrons, ions, and neutral atoms. This is often the case for plasmas, where a chemical model like the Saha equation is used for the computation of the free electron density [67]. However, in WDM it is usually not possible to clearly segregate free and bound electrons and, thus, any concept based on the Lindhard function (i.e., the free-electron gas) requires the introduction of an effective free electron density (or an effective

ionization degree). This is commonly used as a fit parameter to describe experimental XRTS data [25,64–66]. We further note that the effective free-electron density is also used to compute $G(\mathbf{q}, \omega)$ on the basis of some free-electron gas model. In contrast, the LR-TDDFT approach described in Sec. II A does not require the effective free electron density. Moreover, electron-ion interaction effects are included in LR-TDDFT implicitly through the microscopic density inhomogeneity and KS orbitals. Therefore, it is highly beneficial to reformulate Eq. (7) without using the Lindhard function and $G(\mathbf{q}, \omega)$ [equivalently $K_{xc}(\mathbf{q}, \omega)$] of the free-electron gas, but using some $\chi_0(\mathbf{q}, \omega)$ and $K_{xc}(\mathbf{q}, \omega)$ from LR-TDDFT. This is done in the present paper after introducing the method to compute the static XC kernel and KS response function using an external harmonic perturbation in the KS-DFT calculations.

C. Static XC kernel from the direct perturbation approach

The direct perturbation approach is based on the KS-DFT simulation of a system perturbed by an external harmonic potential [48,49,58]. The corresponding electronic Hamiltonian reads [18,35,36,38]

$$\hat{H}_{\mathbf{q},A} = \hat{H}_e + 2A \sum_{j=1}^{N} \cos(\mathbf{q} \cdot \hat{\mathbf{r}}_j), \tag{10}$$

where $\hat{H}_e$ is the Hamiltonian of the unperturbed system. The static external potential is defined by its wave vector $\mathbf{q}$ and amplitude A. The discussion of the general case of a time=dependent external potential can be found in Ref. [18].

The simulation of both the unperturbed ($A = 0$) and perturbed ($A \neq 0$) systems allows one to find a change in the single-electron density:

$$\Delta n_e(\mathbf{r})_{\mathbf{q},A} = \langle n_e(\mathbf{r}) \rangle_{\mathbf{q},A} - \langle n_e(\mathbf{r}) \rangle_{A=0}. \tag{11}$$

In WDM experiments, XRTS measurements are performed on macroscopic objects. With regard to a macroscopic disordered system, what the x-ray probe sees statistically is a large ensemble of atomic position configurations. Therefore, in practice, we perturb a system along a given direction and compute the average $\langle ... \rangle$ along all other directions. Depending on the system temperature and density, one might need further averaging over different atomic configurations. We note that it does not mean that we neglect the local field effects (see Sec. II D). For such disordered systems, the contributions from the density Fourier components to $\Delta n_e(\mathbf{r})_{\mathbf{q},A}$ at $\mathbf{q} + \mathbf{G}$, $\mathbf{q} + 2\mathbf{G}$, etc. are negligible [34]. Physically, it becomes obvious if we recall that, for disordered systems (like molten metals), $\mathbf{G}$ does not describe the Fourier transform of the Bravais lattice but appears due to periodic boundary conditions (with $|\mathbf{G}| = 2\pi/L$) introducing a certain finite-size effect, which we discuss in Secs. III and IV. Furthermore, if the perturbation amplitude A is small enough, one can also neglect the excitation of higher harmonics due to the nonlinear response terms at $2\mathbf{q}$, $3\mathbf{q}$, etc. [39,68,69]. Therefore, the induced density change is described by the linear density response function $\chi(\mathbf{q}) = \chi(\mathbf{q}, \omega = 0)$ in the static limit according to the relation [69]

$$\Delta n_e(\mathbf{r})_{\mathbf{q},A} = 2A \cos(\mathbf{q} \cdot \mathbf{r}) \chi(\mathbf{q}). \tag{12}$$

Similarly, a static KS response function describes the response of the electron density to a change of the KS potential:

$$\Delta n_e(\mathbf{r})_{\mathbf{q},A} = \chi_{KS}(\mathbf{q}) \Delta v_{KS}(\mathbf{r})_{\mathbf{q},A}, \tag{13}$$

where $\Delta v_{KS}(\mathbf{r})_{\mathbf{q},A}$ is the change of the KS potential due to an external perturbation:

$$\Delta v_{KS}(\mathbf{r})_{\mathbf{q},A} = \langle v_{KS}(\mathbf{r}) \rangle_{\mathbf{q},A} - \langle v_{KS}(\mathbf{r}) \rangle_{A=0}. \tag{14}$$

Therefore, the direct perturbation approach provides access to both the macroscopic density response function and the KS response function of a homogeneous system. We reiterate that this method is valid for any disordered system that becomes homogeneous on average; e.g., due to averaging over an ensemble of atomic configurations (snapshots).

Now, we can set $\chi_0(\mathbf{q}, \omega) = \chi_{KS}(\mathbf{q}, \omega)$ and invert Eq. (7) to find the static XC kernel for a homogeneous system [47],

$$K_{xc}(\mathbf{q}) = -\left\{ v(q) + \left(\frac{1}{\chi(\mathbf{q})} - \frac{1}{\chi_{KS}(\mathbf{q})} \right) \right\}$$

$$= \frac{1}{\chi_{RPA}(\mathbf{q})} - \frac{1}{\chi(\mathbf{q})}, \tag{15}$$

where $\chi_{RPA}(\mathbf{q})$ is the screened version of $\chi_{KS}(\mathbf{q})$:

$$\chi_{RPA}(\mathbf{q}, \omega) = \frac{\chi_{KS}(\mathbf{q}, \omega)}{1 - v(q)\chi_{KS}(\mathbf{q}, \omega)}. \tag{16}$$

D. Connection between LR-TDDFT and direct perturbation approach

To access the macroscopic density response function $\chi(\mathbf{q})$ [defined according to Eq. (12)] without applying an external harmonic perturbation, we use the macroscopic dielectric function Eq. (3) in Eq. (6) to find the LR-TDDFT result for $\chi(\mathbf{q})$:

$$\chi(\mathbf{q}, \omega) = \frac{1}{v(q)} \left(\varepsilon_M^{-1}(\mathbf{q}, \omega) - 1 \right). \tag{17}$$

Using Eq. (17), we can compute the macroscopic static density response function $\chi(\mathbf{q}) = \chi(\mathbf{q}, \omega = 0)$ using LR-TDDFT and compare it with $\chi(\mathbf{q})$ from the direct perturbation approach. In Sec. IV A, we show numerical results confirming that the results for $\chi(\mathbf{q})$ from the direct perturbation approach Eq. (12) are equivalent to the LR-TDDFT result computed using Eq. (17).

To get access to the macroscopic KS response function $\chi_{KS}(\mathbf{q}, \omega)$ [defined according to Eq. (12)] without perturbing by an external harmonic potential, we perform the LR-TDDFT calculations without an XC kernel and use the macroscopic dielectric function in the RPA $\varepsilon_M^{RPA}(\mathbf{q}, \omega)$ from Eq. (5) in Eq. (9):

$$\chi_{KS}(\mathbf{q}, \omega) = \frac{1}{v(q)} \left(1 - \varepsilon_M^{RPA}(\mathbf{q}, \omega) \right). \tag{18}$$

We note that the macroscopic KS response function $\chi_{KS}(\mathbf{q}, \omega)$ introduced by Eq. (18) involves the solution of the Dyson-type Eq. (4). In the LR-TDDFT language, this means that $\chi_{KS}(\mathbf{q}, \omega)$ has more information about the ion-induced density inhomogeneity compared to the noninteracting density response function $\chi_{GG}^0(\mathbf{q}, \omega)$. In Sec. IV A, we compute $\chi_{KS}(\mathbf{q})$ using Eq. (18) and compare it with $\chi_{KS}(\mathbf{q})$ from
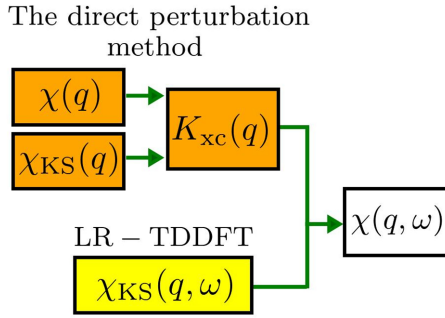
FIG. 1. Computation scheme for the macroscopic density response function Eq. (19) based on the adiabatic (static) XC kernel from the direct perturbation approach Eq. (15) and the macroscopic KS response function Eq. (18) from the LR-TDDFT. The presented self-consistent calculation scheme can be used beyond ALDA with any XC functional across Jacob's ladder.

Eq. (13) to show that the macroscopic static KS response function $\chi_{KS}(\mathbf{q})$ from the direct perturbation approach is in agreement with the LR-TDDFT result.

E. LR-TDDFT calculations of the macroscopic density response function with a consistent static XC kernel

The workflow of LR-TDDFT requires KS orbitals from converged equilibrium KS-DFT simulations. These orbitals are used in the Dyson-type Eq. (2) together with the microscopic XC kernel $K_{G_1,G_2}^{xc}(\mathbf{q}, \omega)$ to compute the density response function, with the microscopic XC kernel being the first-order functional derivative of the XC potential. Consistent LR-TDDFT simulations require a microscopic XC kernel that is fully compatible with the XC functional used to compute the XC potential. However, the LR-TDDFT for extended systems (using the first-order functional derivative of the XC potential to find the XC kernel) currently has the limitation that consistent simulations can be performed using only adiabatic LDA and GGA microscopic XC kernels [55]. For a macroscopic density response function and dielectric function, we can circumvent this limitation for on-average-homogeneous systems (e.g., WDM, dense plasmas, and liquid metals) by combining the static macroscopic XC kernel $K_{xc}(\mathbf{q})$ from the direct perturbation approach, Eq. (15), with the dynamic macroscopic KS response function $\chi_{KS}(\mathbf{q}, \omega)$ defined by Eq. (18).

Our *adiabatic (static) approximation* for the macroscopic density response function reads

$$\chi(\mathbf{q}, \omega) = \frac{\chi_{KS}(\mathbf{q}, \omega)}{1 - [v(q) + K_{xc}(\mathbf{q})]\chi_{KS}(\mathbf{q}, \omega)}, \qquad (19)$$

The self-consistent calculation method represented by Eq. (19) is schematically explained in Fig. 1. To deliver a macroscopic dynamic density response function in the adiabatic approximation, this approach combines the static XC kernel from the direct perturbation approach defined by Eq. (15) with the macroscopic KS response function from LR-TDDFT introduced by Eq. (18). We reiterate that neither Eq. (18) for $\chi_{KS}(\mathbf{q}, \omega)$ nor Eq. (15) for $K_{xc}(\mathbf{q})$ require information about the microscopic XC kernel $K_{G_1,G_2}^{xc}(\mathbf{q}, \omega)$. In this way, we can compute the macroscopic density response function $\chi(\mathbf{q}, \omega)$ in an adiabatic approximation for any available

XC functional in a fully self-consistent manner. The macroscopic dynamic dielectric function follows from Eq. (6).

Importantly, if a consistent adiabatic XC kernel is used, a standard LR-TDDFT result for $\varepsilon_M(\mathbf{q}, \omega)$ as defined by Eq. (3) is equivalent to the result from our adiabatic approximation for the macroscopic density response function Eq. (19). We demonstrate it for the ALDA for the example of warm dense hydrogen in Sec. IV A. By consistency, we mean that the same XC functional is used for calculating the KS response function as well as for the XC kernel.

For real materials, the adiabatic approximation represented by Eq. (19) is more powerful than ALDA or AGGA of the standard LR-TDDFT since Eq. (19) can be computed using any XC functional across Jacob's ladder of DFT [70,71]. For example, Moldabekov *et al.* [34] used the direct perturbation approach for the investigation of the static density response function and XC kernel of the UEG and warm dense hydrogen using various LDA, GGA, and meta-GGA functionals. Additionally, different hybrid XC functionals have been analyzed at WDM conditions using the UEG model in Refs. [51,52]. These prior works used the reference static density response function $\chi_0(q)$ from KS-DFT calculations with zero XC functional. This has been done for benchmarking purposes against available QMC results. The uniqueness of Eq. (19) is the consistent way to compute $\chi_0(\mathbf{q}, \omega) = \chi_{KS}(\mathbf{q}, \omega)$ and $K_{xc}(q)$ for applications within the adiabatic (static) approximation.

For WDM and dense plasma applications, Eq. (19) does not require the introduction of an effective free electron density (in contrast to Lindhard-function-based approaches) and our static XC kernel is now material specific. This also eliminates the need for using some model LFC in Eq. (8).

We note that for the UEG, $\chi_{KS}(\mathbf{q}, \omega)$ reduces to the Lindhard function as we show in Sec. IV A. In this case, QMC simulations have shown that the adiabatic (static) approximation is highly accurate in the case of weak to moderate coupling strengths, e.g., at metallic densities [72].

III. SIMULATION PARAMETERS

We use Hartree atomic units for all numerical results presented in this paper. The total density of electrons is given in terms of the density parameter $r_s = (4\pi n/3)^{-1/3}$, which is the mean-interparticle distance. We note that r_s also represents the characteristic coupling parameter between electrons [19,73,74]. The temperature of electrons is expressed in terms of the degeneracy parameter $\theta = T/T_F$, which is the temperature value in the units of the Fermi temperature (energy). We consider $r_s = 2$ and $r_s = 4$, which are typical for WDM experiments. For warm dense hydrogen, we set $\theta = 1$. This allows us to compare $\chi(q)$ from the KS-DFT simulations with the recent exact path integral QMC results by Böhme *et al.* [68].

To test the validity of the presented approach for $\chi_{KS}(q)$ in the limit of the UEG, we also use $\theta = 1$, 0.5, and 0.01.

We set $\mathbf{q}$ along the z axis and, having this in mind, we drop vector notation. In the case of the direct perturbation approach, the perturbation wave numbers are given by $q = j \cdot q_{min}$ with $q_{min} = 2\pi/L$ and j being positive integers. For a given snapshot of ionic positions, the density and KS potential perturbations were averaged along the x and y axes

(since **q** is along the z axis). The size of the main simulation box is defined by $n_0 L^3 = N$, where $n_0 = 3/(4\pi r_s^3)$ and N is the total number of electrons in the main simulation box. We consider $N = 14$ and $N = 20$. At the considered parameters, the finite size effects at $N = 14$ and $N = 20$ are negligible. This was demonstrated by path integral QMC simulations in Refs. [68,69,75,76] and by KS-DFT simulations in Refs. [34,51,77,78].

In the case of the LR-TDDFT calculations, q values must be the difference between two k-points. For example, if the k-point grid is $N_k \times N_k \times N_k$, the wave number is given by $\mathbf{q} = (l/N_k, m/N_k, p/N_k) 2\pi/L$, where l, m, p are positive integer numbers and are not multiples of N_k. Since we set **q** along the z axis, we always have $l = 0$ and $m = 0$.

The external field amplitude in the direct perturbation approach must be small enough so the density perturbation can be described by the LRT. For warm dense hydrogen, we set $A = 0.01$ (in Hartree). It was shown to be within the LRT domain in Ref. [68]. Following Ref. [39], for the UEG calculations, we set $A = 0.01$ at $r_s = 2$ and $A = 0.002$ at $r_s = 4$.

For the KS-DFT calculations of the static XC kernel, we use the ABINIT package [79–84] with the pseudopotentials by Goedecker *et al.* [85]. In the case of the LDA functional [86], we cross checked that the ABINIT results are reproduced by the KS-DFT calculations using the GPAW code [87–90], which is a real-space implementation of the projector augmented-wave method. For the LR-TDDFT calculations on the basis of the LDA, we used the GPAW code for the calculation of the density response function and KS response function [91]. The ionic configurations have been obtained from thermal KS-DFT-based molecular dynamics simulations as it is described in Ref. [92].

The direct perturbation approach based KS-DFT simulations of warm dense hydrogen were performed for 14 (with 280 bands) and 20 (with 400 bands) particles in the main simulation cell. We used $10 \times 10 \times 10$ k-point sampling and 30 Ha energy cutoff. For the LR-TDDFT calculations of the static density response functions at $r_s = 2$ and $q < 2q_F$, we used 14 electrons in the main cell with 280 bands and 500 eV energy cutoff in the equilibrium-state calculations. For $q > 2q_F$, we used the equilibrium state calculations with 1500 bands for 14 electrons in the main cell, $4 \times 4 \times 4$ k points, and 550 eV energy cutoff. Using wave functions from the equilibrium state, the LR-TDDFT calculations were performed with the cutoff in the dielectric function set to 100 eV and the broadening parameter $\eta = 0.001$.

The calculations for the static density response functions of the UEG at $\theta = 0.01$ and $\theta = 0.5$ were performed using $N = 38$ particles in the main cell (with 44 bands), $10 \times 10 \times 10$ k-point sampling, and 30 Ha energy cutoff. The data for $\theta = 1$ is obtained using $N = 20$ electrons in the main cell (with 400 bands), $10 \times 10 \times 10$ k-point sampling, and 30 Ha energy cutoff.

We note that in the case of the UEG, Moldabekov *et al.* [51,77] benchmarked the quality of different LDA, GGA, meta-GGA, and hybrid-level XC functionals within thermal KS-DFT against an exact QMC data in the ground state and at parameters considered in this paper. Similarly, in the case of warm dense hydrogen, in Refs. [34,68], the accuracy of several LDA, GGA, and meta-GGA-level XC functionals has
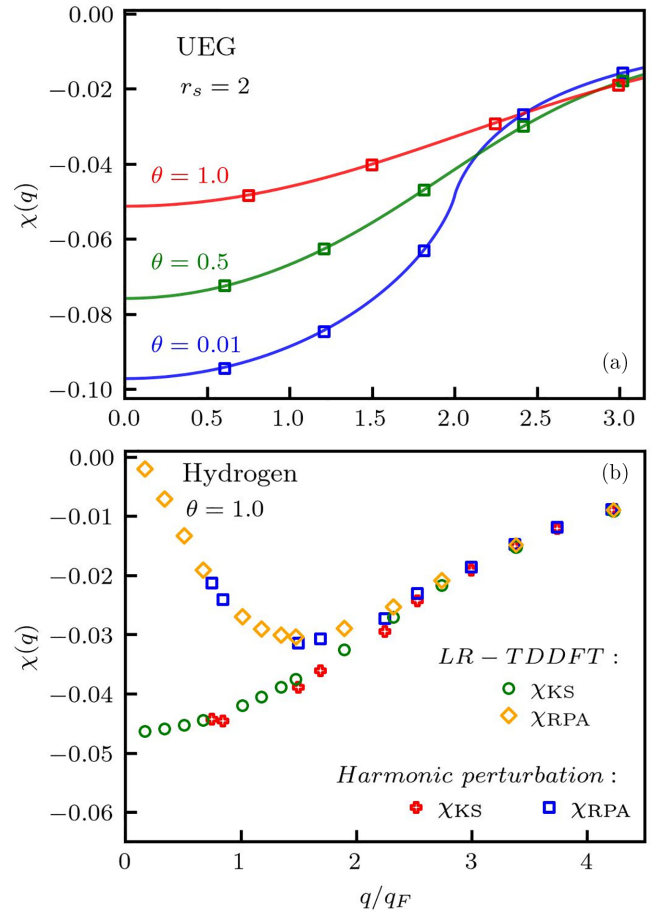

FIG. 2. (a) Symbols show KS response function computed from the KS-DFT simulations of the UEG with LDA XC functional for $r_s = 2$ at different values of the reduced temperature θ. Solid lines are corresponding results computed using the Lindhard function. (b) KS response function and corresponding RPA values for warm dense hydrogen at $r_s = 2$ and $\theta = 1$ as computed using the LR-TDDFT (green and orange symbols) and from the direct perturbation technique (red and blue symbols).

been analyzed using QMC data. The convergence of KS-DFT simulations with respect to such computation parameters as k-point grid, energy cutoff, the number of particles, and the number of bands have been studied in these works for UEG [51,77] and warm dense hydrogen [34,68]. In this paper, we choose the same or better (such as larger k-point grid and energy cutoff) computation parameters to ensure the convergence of the presented results. For the UEG, the convergence of KS-DFT simulations is confirmed by reproducing an exact Lindhard response function in the thermodynamic limit (see top panels in Figs. 2 and 3 and related discussion in Sec. IV). In the case of warm dense hydrogen, the high quality of the KS-DFT simulations is confirmed on the example of LDA XC functional by comparing to the QMC data for the density response (see Fig. 4 and discussion in Sec. IV).

IV. SIMULATION RESULTS

A. Equivalence of LR-TDDFT and the direct perturbation-based approach

To test the correctness of the macroscopic KS response function computed using Eq. (13), first we consider the UEG
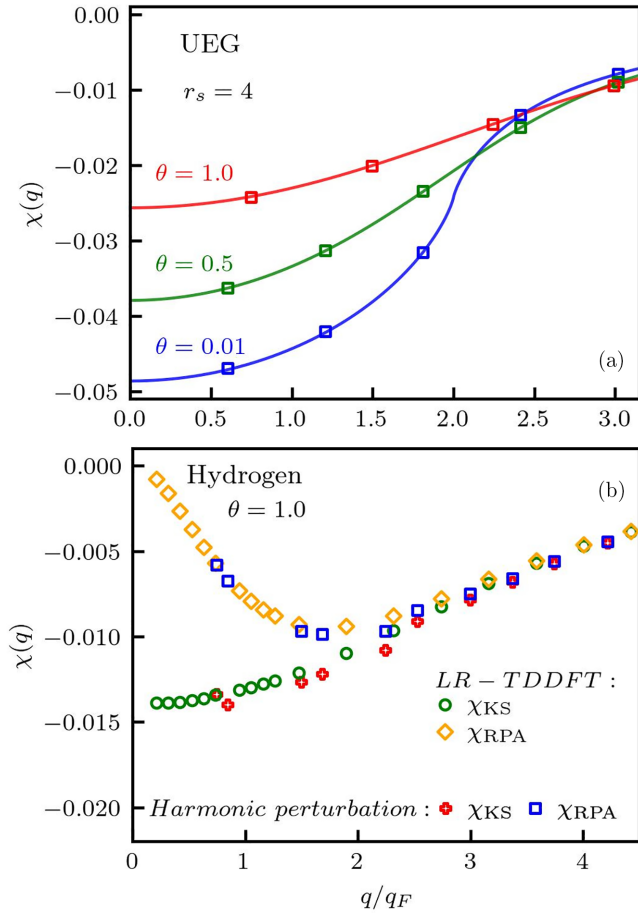
FIG. 3. (a) Symbols show KS response function computed from the KS-DFT simulations of the UEG with LDA XC functional for $r_s = 4$ at different values of the reduced temperature θ. Solid lines are corresponding results computed using the Lindhard function. (b) KS response function and corresponding RPA values for warm dense hydrogen at $r_s = 4$ and $\theta = 1$ as computed using the LR-TDDFT (green and orange symbols) and from the direct perturbation technique (red and blue symbols).
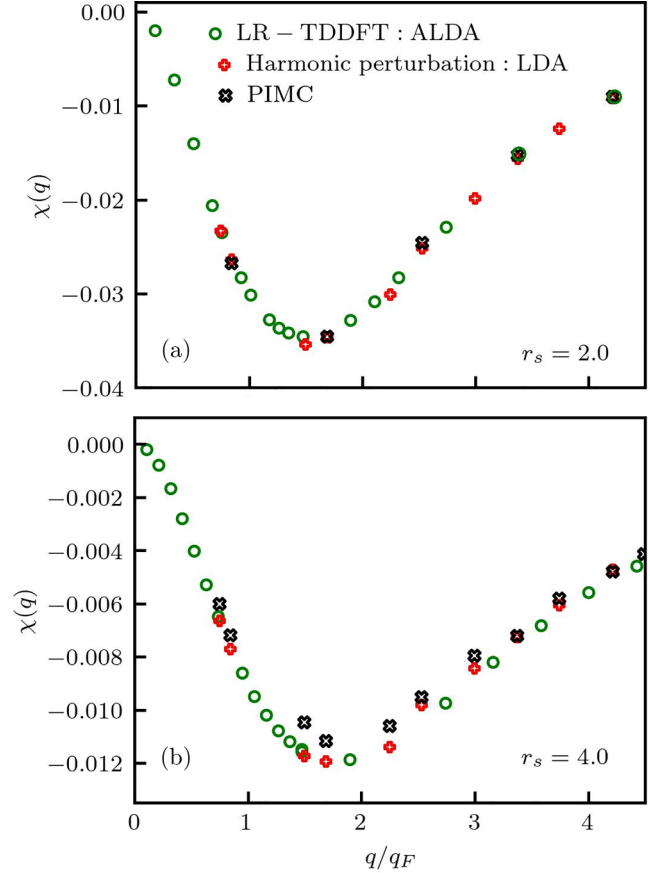

FIG. 4. Density response function of warm dense hydrogen at (a) $r_s = 2$ and (b) $r_s = 4$ for $\theta = 1$. The results computed using the LR-TDDFT with ALDA kernel and the harmonic perturbation-based approach using LDA functional are compared with the exact PIMC data from Ref. [68].

[19] for which the macroscopic KS response function must be equivalent to the Lindhard function. We show that it is indeed the case for $r_s = 2$ in Fig. 2(a) and for $r_s = 4$ in Fig. 3(a) with θ covering both the ground state and the WDM regime. From Figs. 2(a) and 3(a), we see that the macroscopic KS response function Eq. (13) perfectly reproduces the Lindhard function in the thermodynamic limit for the UEG. To get the data presented in these figures, we used the LDA functional by Perdew and Wang [93]. Therefore, Eq. (13) provides the correct noninteracting (ideal) response function even if the KS-DFT calculations are performed with the nonzero XC functional.

Second, in Figs. 2(b) and 3(b), we demonstrate that the macroscopic static KS response function of warm dense hydrogen at $\theta = 1$ computed using the direct perturbation approach Eq. (13) is equivalent to the result found using the standard LR-TDDFT method via Eq. (18). Figures 2(b) and 3(b) present results for $r_s = 2$ and 4, respectively, at $\theta = 1$. Additionally, we show the results in the RPA, which are computed using $\chi_{KS}(q)$ in Eq. (7) with $\omega = 0$. From Figs. 2(b)

and 3(b), one can see that the $\chi_{KS}(q)$ computed using Eq. (13) is in agreement with the $\chi_{KS}(q)$ obtained using Eq. (18).

Next, we show in Fig. 4 that the density response function $\chi(q)$ computed according to Eq. (13) within the direct perturbation approach using the LDA XC functional is in agreement with the $\chi(q)$ from the LR-TDDFT calculations using the ALDA kernel and equilibrium state wave functions generated using LDA. Figure 4(a) shows the data for $r_s = 2$ and Fig. 4(b) presents the results for $r_s = 4$. Additionally, in Fig. 4, we compare the KS-DFT results for $\chi(q)$ with the recent exact path-integral quantum Monte Carlo (PIMC) results [68]. From Fig. 4(a), one can see that the KS-DFT results are in close agreement with the PIMC data at $r_s = 2$. In Ref. [68], it was shown that at $\theta = 1$ and $r_s = 2$, electrons in the warm dense hydrogen manifest free-electron-like behavior, indicating weak electron-ion coupling. In contrast, at $r_s = 4$ and $\theta = 1$, electron-ion coupling is strong and the system can effectively be described as partially ionized. As a result, in Fig. 4(b), we observe that the quality of the LDA based KS-DFT data around $2q_F$ significantly deteriorates compared to the exact PIMC data with the decrease in the density from $r_s = 2$ to $r_s = 4$. The deterioration of the quality of the LDA-based description with the decrease in density is due to
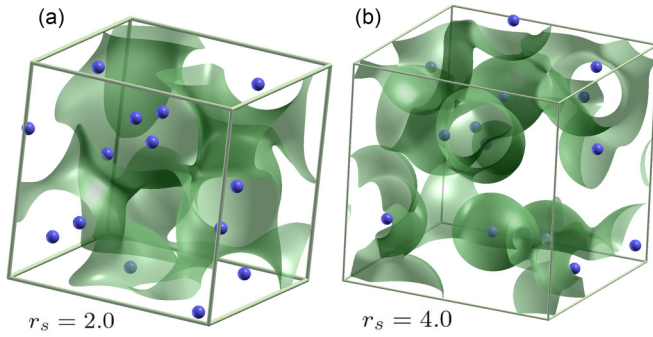
FIG. 5. Illustration of the stronger localization of the electrons around protons with the decrease in density from (a) $r_s = 2$ to (b) $r_s = 4$ at fixed $\theta = 1$ using an isosurface of the electronic density as obtained from DFT-MD. This figure was created using XCrySDen [96,97].

the stronger localization of electrons around ions [94], which gives rise to self-interaction errors in KS-DFT [95]. Stronger coupling between electrons and ions also leads to the smaller density response amplitude as can be seen by comparing the $\chi(q)$ values in Figs. 4(a) and Fig. 4(b). The stronger localization of electrons around ions at $r_s = 4$ compared to the case

with $r_s = 2$ in warm dense hydrogen is illustrated using an isosurface of the electronic density in Fig. 5.

The third quantity we consider is the macroscopic dynamic dielectric function $\varepsilon_M(q, \omega)$ of warm dense hydrogen. We compute $\varepsilon_M(q, \omega)$ using the standard LR-TDDFT with the ALDA kernel and LDA-based KS orbitals. Additionally, we calculate $\varepsilon_M(q, \omega)$ using $\chi(q, \omega)$ from Eq. (19) in Eq. (6) according to the scheme presented in Fig. 1, where $\chi_{KS}(q, \omega)$ is computed using Eq. (18) and the LDA XC kernel is obtained from the direct perturbation approach using Eq. (15). The comparison of the data for $\varepsilon_M(q, \omega)$ computed using these two different ways is presented in Fig. 6, where we show the real and imaginary parts of $\varepsilon_M(q, \omega)$ at $q \simeq 0.873 q_F$ and $q \simeq 1.434 q_F$. Additionally, in Fig. 6, we present the RPA results computed using zero XC kernel. From Fig. 6, we observe that the ALDA based LR-TDDFT data for $\varepsilon_M(q, \omega)$ is in excellent agreement with the result obtained using $\chi(q, \omega)$ from Eq. (19) in Eq. (6).

Therefore, for the example of the warm dense hydrogen, we have demonstrated using the LDA functional that our approach from Eq. (19) for the macroscopic $\chi(q, \omega)$ is equivalent to the standard LR-TDDFT with an adiabatic XC kernel approximation. We reiterate that the strength of the presented approach is that it can be used with the static XC kernel
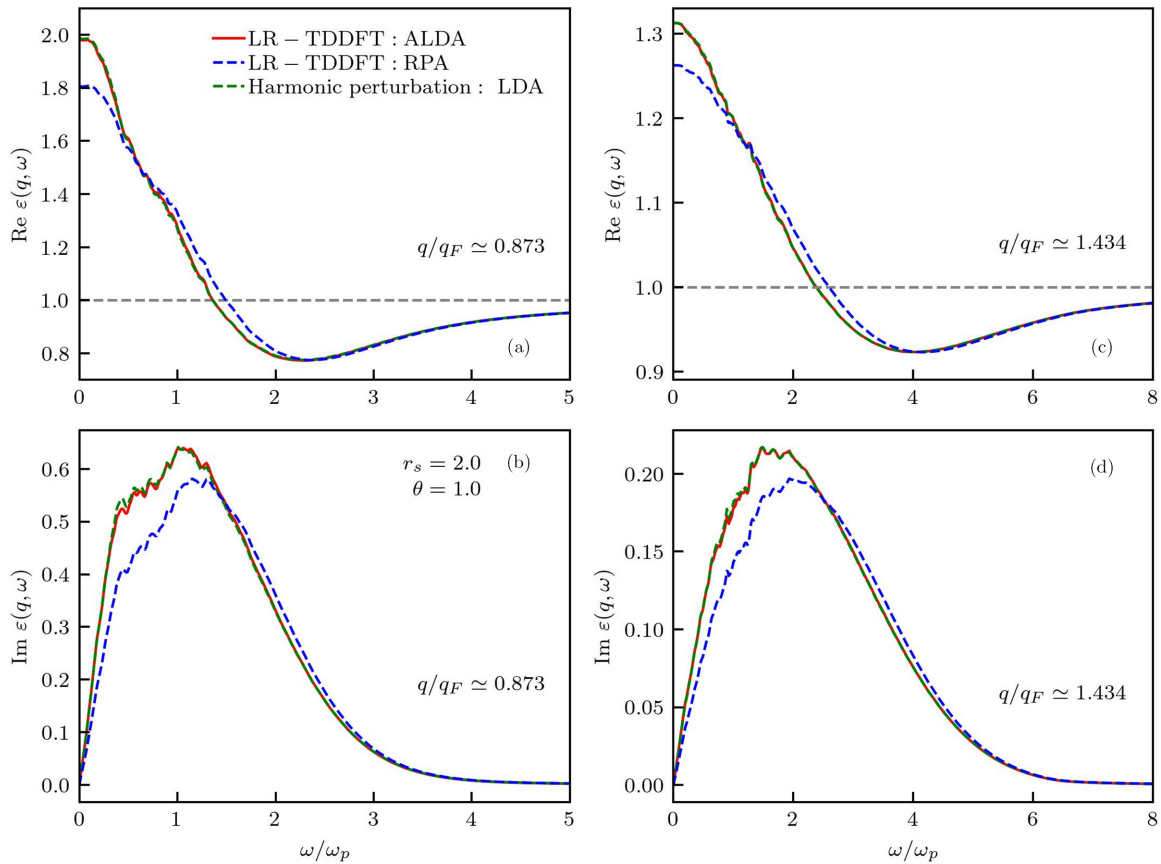

FIG. 6. Demonstration of the equivalence of the LR-TDDFT result with the ALDA kernel (solid red line) to the macroscopic XC kernel and macroscopic KS response function based scheme (as explained in Fig. 1) using the LDA functional (dashed green). The results are presented for warm dense hydrogen at $r_s = 2$ and $\theta = 1$. (a) The real part of the dynamic dielectric function and (b) the imaginary part of the dynamic dielectric function at $q/q_F \simeq 0.873$. (c) The real part of the dynamic dielectric function and (d) the imaginary part of the dynamic dielectric function at $q/q_F \simeq 1.434$. The RPA result is provided for comparison as well (dashed blue).

of any available XC functional without explicitly computing the second-order functional derivative. For example, using the direct perturbation approach, Moldabekov *et al.* [34] presented a static XC kernel for LDA, GGA, and meta-GGA level functionals as well as for various hybrid functionals [51,52]. Moreover, Eq. (19) represents a method where the adiabatic XC kernel $K_{XC}(q)$ is fully consistent to the XC functional used to generate the KS response function $\chi_{KS}(q, \omega)$ [defined by Eq. (18)].

B. Static XC kernel for warm dense hydrogen at metallic density

In Ref. [34], the PIMC data-based comparative analysis of the density response function of warm dense hydrogen at $r_s = 2$ and $r_s = 4$ using PBE [98], PBEsol [99], AM05 [100], and SCAN [101] functionals revealed that these XC functionals do not improve the description of the warm dense hydrogen compared to ground state LDA [93] based calculations. Moreover, it was shown that a finite-temperature LDA functional [102] developed for WDM conditions does not improve the quality of the description compared to the ground state LDA and even provides slightly worse results. Among aforementioned functionals in Ref. [34], the meta-GGA level SCAN functional occupies a higher rung on Jacob's ladder compared to the LDA and GGA functionals and is more accurate than the LDA and PBE for the ground state applications. Thus, it is surprising that SCAN performs worse than the ground state LDA and PBE when the thermal energy is comparable with the Fermi energy. It is a natural question to ask whether other meta-GGA functionals have the same drawback in the WDM regime. Thus, in this paper, in addition to the ground-state LDA and PBE, we included another two meta-GGA XC potentials into our analysis. We consider XC potentials introduced by Tran and Blaha [103] (TB) and by Räsänen, Pittalis, and Proetto (RPP) [104]. These potentials are introduced by modifying the Becke–Johnson exchange potential [105] (approximating an exact Hartree-Fock exchange) and by adding the LDA correlation by Perdew and Wang [93]. The TB approximation provides high-quality results for various types of solids and good agreement with experiments. This approximation recovers the ground-state LDA approximation for a constant electronic density. The RPP approximation is designed to be exact for any single-electron system and to reduce to the LDA level description in the limit of a constant density. For example, the RPP approximation proved to be very accurate for a hydrogen chain in an external electric field [104].

We start our discussion of the results for warm dense hydrogen at a metallic density $r_s = 2$. We consider the static KS response function $\chi_{KS}(q)$, the static density response in the RPA $\chi_{RPA}(q)$, and the static total density response function $\chi(q)$. In Fig. 7, we analyze the relative deviation of $\chi_{KS}(q)$, $\chi_{RPA}(q)$, and $\chi(q)$ from the LDA-based data for $r_s = 2$ and $\theta = 1$. The results are presented for 14 and 20 particles in the main cell. The relative deviation from the LDA based data is computed as

$$\Delta\chi_{KS}(q)[\%] = \frac{\chi_{KS}(q) - \chi_{KS}^{LDA}(q)}{\chi_{KS}^{LDA}(q)} \times 100\%, \quad (20)$$
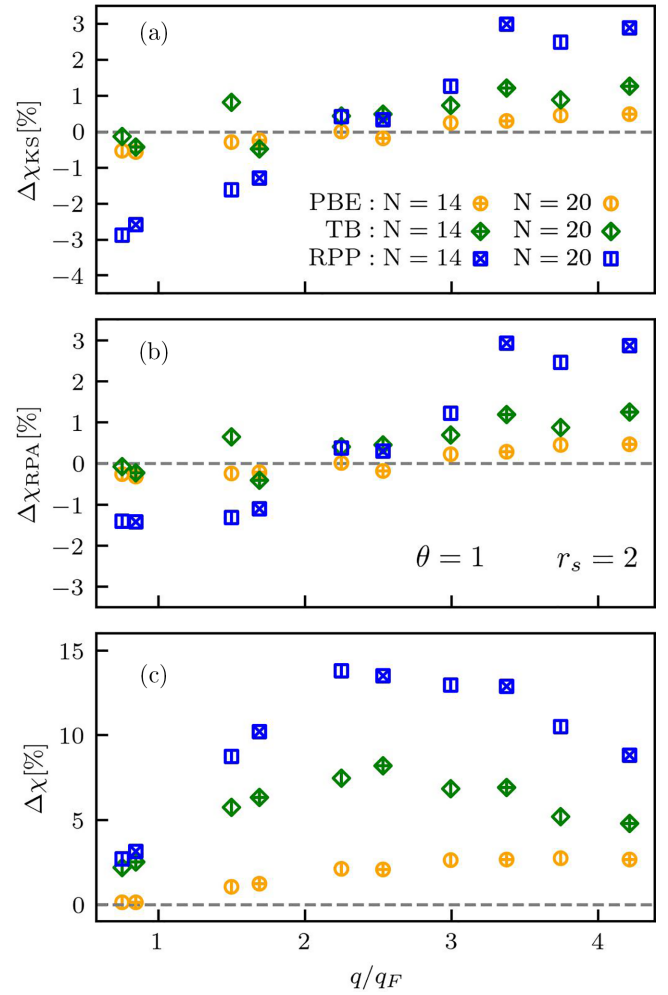

FIG. 7. The relative deviation from the LDA results of (a) the KS response function, (b) the screened response on the level of RPA, and (c) the total density response function from simulations using GGA level PBE functional, meta-GGA-level TB, and RPP approximations for warm dense hydrogen at $r_s = 2$ and $\theta = 1$.

where $\chi_{KS}^{LDA}(q)$ is the static KS response function calculated using the LDA.

Similar expressions are used to evaluate the relative deviations of $\chi_{RPA}(q)$ and $\chi(q)$ from corresponding LDA-based results $\chi_{RPA}^{LDA}(q)$ and $\chi^{LDA}(q)$:

$$\Delta\chi_{RPA}(q)[\%] = \frac{\chi_{RPA}(q) - \chi_{RPA}^{LDA}(q)}{\chi_{RPA}^{LDA}(q)} \times 100\% \quad (21)$$

and

$$\Delta\chi(q)[\%] = \frac{\chi(q) - \chi^{LDA}(q)}{\chi^{LDA}(q)} \times 100\%. \quad (22)$$

Figure 7(a) shows that the PB- and TB-based data for $\chi_{KS}(q)$ are in very close agreement to the $\chi_{KS}^{LDA}(q)$ with the relative deviation smaller than 2% by absolute value. The RPP-based results for $\chi_{KS}(q)$ have slightly larger disagreement with $\chi_{KS}^{LDA}(q)$, which is in between 3% and −3%. These disagreements are further diminished at $q < 2q_F$ due to screening as one can see from Fig. 7(b), where the results for the $\Delta\chi_{RPA}(q)$ are presented. In $\chi_{RPA}(q)$, screening is taken
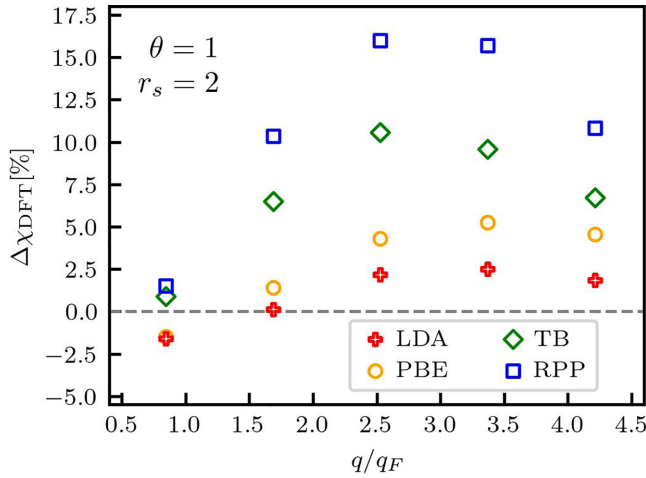
FIG. 8. The deviation of the KS-DFT results from the exact PIMC data for the static density response function of warm dense hydrogen at $r_s = 2$ and $\theta = 1$.

into account using Eq. (7), which neglects the XC kernel. Overall, we see that the results for $\chi_{KS}(q)$ as well as $\chi_{RPA}(q)$ computed using different considered XC potentials are close to each other. In fact, at $r_s = 2$ and $\theta = 1$, $\chi_{KS}(q)$ also has close values to the Lindhard function derived using the ideal electron gas model (see Fig. 2). This is in agreement with previously discussed observation that at $r_s = 2$ and $\theta = 1$ electrons are strongly delocalized.

The results for the actual density response $\chi(q)$ of warm dense hydrogen [cf. Eq. (11)] to an external field are presented in Fig. 7(c). From Fig. 7(c), we see that the $\chi(q)$ computed using the TB and RPP approximations significantly differs from the LDA-based data at $q > q_F$. It is also the case for the PBE-based data for $q > 2q_F$. This is in contrast to the behavior of $\chi_{KS}(q)$ and $\chi_{RPA}(q)$, for which considered XC potentials give nearly the same results. Another important observation from Fig. 7 is that the results computed using 14 and 20 particles exhibit a very similar behavior. This means that the results computed at $r_s = 2$ and $\theta = 1$ using 14 particles in the main cell are not affected by finite-size effects. This further corroborates previous results presented in Refs. [34,68].

In Fig. 8, we analyze the quality of the considered approximations by comparing to the exact PIMC data from Ref. [68] for 14 particles in the main cell. The relative deviation of the KS-DFT data from the PIMC results is computed as

$$\Delta\chi_{DFT}(q)[\%] = \frac{\chi(q) - \chi^{PIMC}(q)}{\chi^{PIMC}(q)} \times 100\%, \quad (23)$$

where $\chi^{PIMC}(q)$ is the density response function from the PIMC simulations using the direct perturbation approach [68].

From Fig. 8, it is clear that the ground-state LDA provides more accurate data for $\chi(q)$ compared to the PBE, TB, and RPP.

In Fig. 9, we present the corresponding results for the static XC kernel. In Fig. 9(a), we show the static XC kernel computed self-consistently from the KS-DFT according to Eq. (15). In Fig. 9(b), we present the static XC kernel obtained using the exact $\chi(q)$ from the PIMC in Eq. (15). For both cases, the $\chi_{KS}(q)$ is found from the KS-DFT simulations
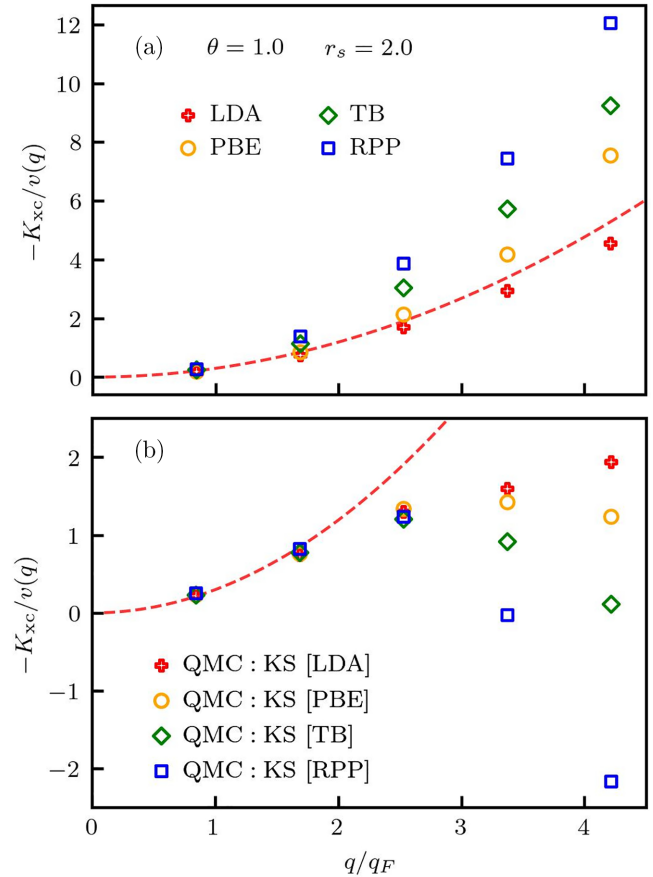

FIG. 9. (a) Fully consistent static XC-kernel from KS-DFT simulations with different XC functionals. (b) Static XC-kernel extracted using the PIMC data and KS-response function from KS-DFT simulations. Demonstration of the equivalence of the KS response function from the harmonic perturbation technique and LR-TDDFT calculations. The results are for warm dense hydrogen at $r_s = 2$ and $\theta = 1$.

according to Eq. (13). The dashed red line in Fig. 9 represents a quadratic dependence of the LFC $G(q)$ in Eq. (8) (i.e., the long-wavelength approximation) according to the compressibility sum rule [34].

From Fig. 9(a), one can see that the PBE, TB, and RPP results for the XC kernel converge to the LDA-based result at small wave numbers $q < 2q_F$ and deviate with the increase in the wave number at $q > 2q_F$. At considered wave numbers, the LDA-based data closely follows the quadratic dependence. This is also the case for the PIMC-based XC kernel at $q < 2q_F$ as one can see in Fig. 9(b). We observe that the XC kernels computed at $q < 2q_F$ using the LDA, PBE, TB, and RPP based $\chi_{KS}(q)$ are in a perfect agreement with the long-wavelength approximation, i.e., they have a quadratic dependence. However, these XC kernels show a strong deviation from the quadratic dependence toward lower values with the increase in the wave number at $q > 2q_F$. Furthermore, if one compares the position of the PBE-, TB-, and RPP-based results relative to the dashed red line in Figs. 9(a) and 9(b), we see that the corresponding XC kernel values deviate in different directions from the quadratic dependence in Figs. 9(a) and Fig. 9(b). Overall, from comparing results in Figs. 9(a)
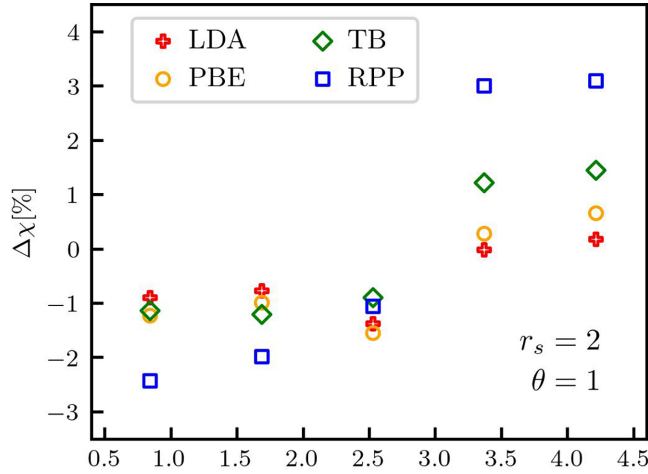
FIG. 10. Inaccuracy in the density response function due to an inconsistent combination of the KS response function and the XC kernel extracted from the PIMC data and an ideal reference function without XC effects. The results are for warm dense hydrogen at $r_s = 2$ and $\theta = 1$.

and 9(b), we conclude that the LDA, PBE, TB, and RPP give accurate results for the XC kernel at $q < 2q_F$. At $q > 2q_F$, the PBE, TB, and RPP fail to describe the XC kernel not only quantitatively, but also qualitatively.

Another interesting question is whether it is possible to devise an universal XC kernel that can be used in the LR-TDDFT in combination with $\chi_{KS}(q)$ to closely reproduce exact data for the density response properties in a wide range of parameters (temperatures, densities, and wave numbers). Our analysis of the static density response function and XC kernel indicates that there is no such universal XC kernel for real materials. One of many reasons could be that $\chi_{KS}(q)$ depends on the used approximation for the XC potential. We observe it to a lesser extent at $r_s = 2$ and to a greater extent at $r_s = 4$ (as we show in Sec. IV C), but it is always the case. In other words, the XC effects are included into both $\chi_{KS}(q)$ and $K_{xc}(q)$. To mitigate this effect, we computed $\chi_{KS}(q)$ with the XC functional set to zero. We denote the corresponding KS response function as $\chi_{KS}^{NXC}(q)$ (with NXC standing for null XC). We note that in this case we have noninteracting electrons in an external field of ions. Then we use $\chi_{KS}^{NXC}(q)$ in combination with the exact PIMC data for $\chi(q)$ in Eq. (15) to compute $K_{xc}(q)$. The computed XC kernel is then combined with the $\chi_{KS}(q)$ computed using nonzero XC functional (the LDA, PBE, TB, and RPP) to find the density response function $\chi(q)$ using Eq. (19). We see from Fig. 10 that the deviation of the $\chi(q)$ computed in this way from the exact PIMC data is a few percent, but not zero. Thus, it does not reproduce the exact PIMC results for $\chi(q)$. However, we note that the error in the $\chi(q)$ in Fig. 10 is significantly smaller than deviations shown in Fig. 8. This indicates that at $r_s = 2$ and $\theta = 1$, the $\chi_{KS}^{NXC}(q)$ is a good universal reference function for the computation of the XC kernel using the exact data for $\chi(q)$. We connect this finding to the fact that at $r_s = 2$ and $\theta = 1$, the warm dense hydrogen is nearly fully ionized and electron properties are similar to that of free electron gas. Indeed, we show in Sec. IV C that strong electronic localization around ions at
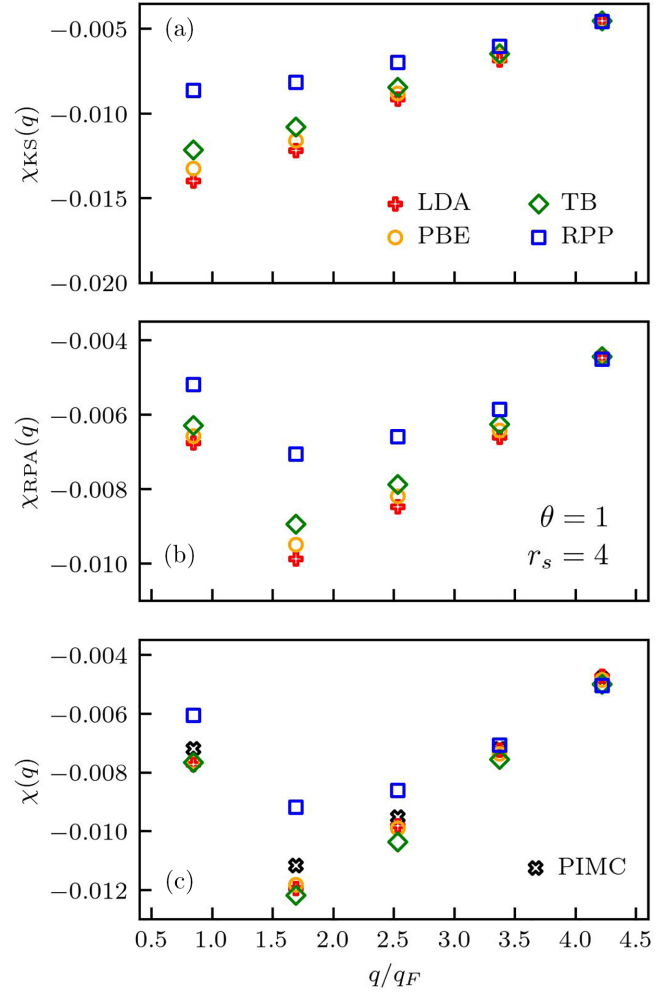

FIG. 11. (a) The KS response function, (b) the screened response on the level of RPA, and (c) the total density response function from simulations using LDA, PBE, and meta-GGA level TB and RPP approximations for warm dense hydrogen at $r_s = 4$ and $\theta = 1$.

$r_s = 4$ leads to a significant worsening of the $\chi_{KS}^{NXC}(q)$-based approach.

C. Static XC kernel for strongly correlated warm dense hydrogen

Now we consider warm dense hydrogen at $r_s = 4$ and $\theta = 1$. At these parameters, we have a stronger electron-electron as well as electron-ion coupling compared to the case with $r_s = 2$ and $\theta = 1$. The results for $\chi_{KS}(q)$, $\chi_{RPA}(q)$, and $\chi(q)$ are presented in Fig. 11 (with 14 particles in the main cell). From Fig. 11(a), one can see that there are strong disagreements between $\chi_{KS}(q)$ values computed using the LDA, PBE, TB, and RPP at $q < 3q_F$. For $\chi_{RPA}(q)$, these disagreements are somewhat alleviated due to screening, as we see from Fig. 11(b). The results for the total density response function $\chi(q)$ are presented in Fig. 11(c), where we provide a comparison with the exact PIMC data. From Fig. 11(c), we see the LDA- and PBE-based data have a similar quality compared to the exact PIMC data. The TB-based data is slightly worse than LDA and PBE. The results computed using RPP approximation
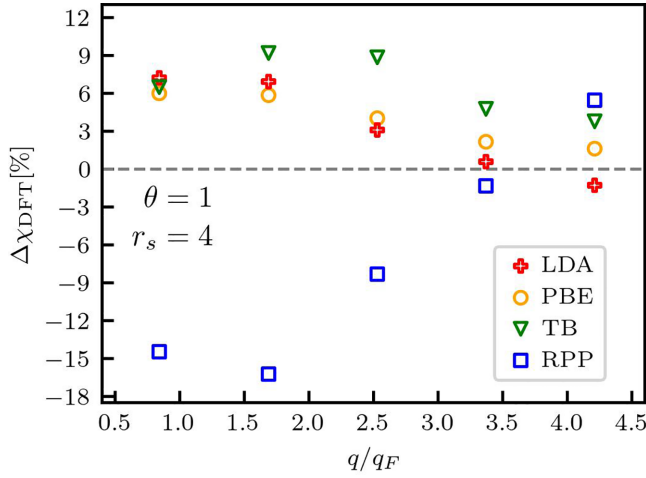
FIG. 12. The deviation of the KS-DFT results from the exact PIMC data for the static density response function of warm dense hydrogen at $r_s = 4$ and $\theta = 1$.

show largest disagreement with the PIMC data. Overall, the presented KS-DFT results have their largest deviation from the PIMC data around $1.5 q_F < q < 2q$.

We further quantify the difference between the KS-DFT data and the PIMC results using $\Delta \chi_{\rm DFT}$ defined by Eq. (23). The results for the relative difference $\Delta \chi_{\rm DFT}$ are presented in Fig. 12. From Fig. 12, we observe that the LDA- and PBE-based data have a similar quality with the largest deviation about 7% at $q \simeq 0.845 q_F$. The quality of the LDA- and PBE-based data improves with the increase in the wave number with a relative disagreement of a few percent at $q \gtrsim 2.5 q_F$. Compared to the LDA and PBE, the results computed using the TB and RPP approximations are significantly worse and cannot be described as reliable at all considered wave numbers.

Let us now consider the effect of the approximation used for the XC potential on the $\chi_{\rm KS}(q)$ and $\chi_{\rm RPA}(q)$ in more detail. We present the relative deviation of the $\chi_{\rm KS}(q)$ and $\chi_{\rm RPA}(q)$ computed using the PBE, TB, and RPP compared to the LDA based data in Figs. 13(a) and 13(b), respectively. For the calculation of the relative deviations, we used Eqs. (20) and (21). In Fig. 13, we show the results computed for both 20 and 14 particles in the main cell. We note that the values of the RPP data points are reduced by a factor of 4 for a better illustration of the results in Fig. 13. From Fig. 13, one can see that the PBE- and LDA-based results for $\chi_{\rm KS}(q)$ have a difference of about 5% at $q < 2.5 q_F$. This difference monotonically reduces with the increase of the wave number at $q > 2.5 q_F$. Similar behavior is observed from Fig. 13(b) for $\chi_{\rm RPA}(q)$, but with the magnitude of the difference significantly smaller due to screening. The TB- and RPP-based results for $\chi_{\rm KS}(q)$ and $\chi_{\rm RPA}(q)$ are in agreement with the LDA-based data only at large wave numbers $q > 3 q_F$ and drastically differ from the LDA-based results at $q < 3 q_F$.

In Fig. 13(c), we present the relative deviation of the total $\chi(q)$ obtained using the PBE, TB, and RPP approximations compared to the LDA-based results [computed using Eq. (22)]. The first interesting observation is that $\chi(q)$ computed using the TB is in good agreement with the LDA-based
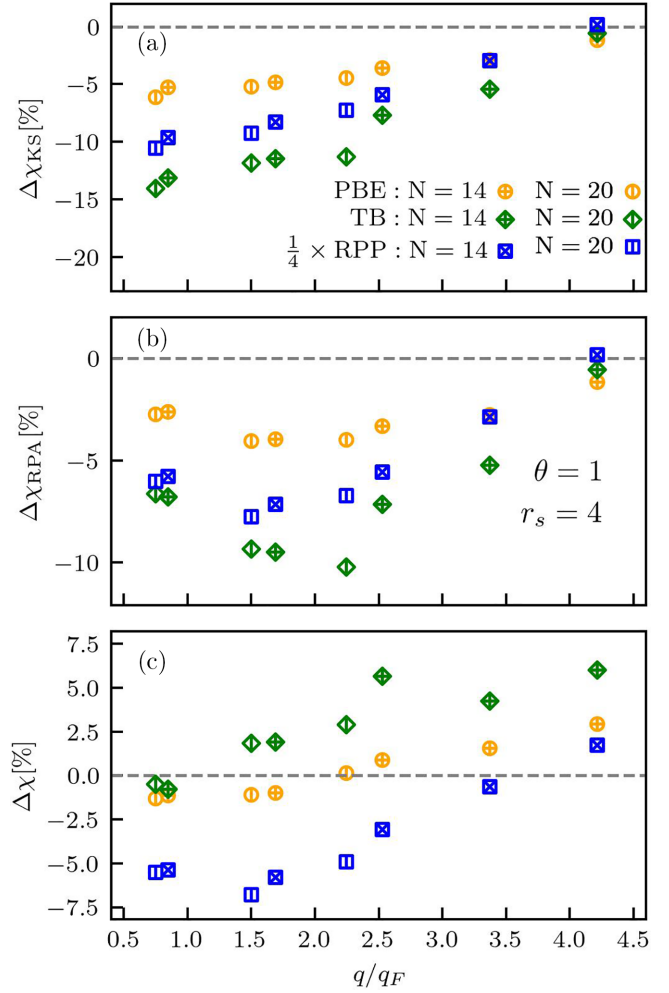

FIG. 13. The relative deviation from the LDA results for (a) the KS response function, (b) the screened response on the level of RPA, and (c) the total density response function from simulations using GGA-level PBE functional, meta-GGA level TB and RPP approximations for warm dense hydrogen at $r_s = 4$ and $\theta = 1$.

result at $q < 2.5 q_F$ (with the difference $\Delta \chi(q) \lesssim 2.5$ %). This is in contrast to the discussed relative differences for $\Delta \chi_{\rm KS}(q)$ in Fig. 13(a). Additionally, the $\Delta \chi(q)$ for the TB-based results increases with the increase in the wave number, while $\Delta \chi_{\rm KS}(q)$ decreases. This clearly demonstrates that $\chi_{\rm KS}(q)$—being an auxiliary quantity—should not be used to gauge the quality of a particular XC functional upon comparing with actual properties of a physical system. The PBE-based data for $\Delta \chi(q)$ show a good agreement with the LDA based results ($\Delta \chi(q) \lesssim 2.5\%$). Overall, the agreement between the PBE-based $\chi(q)$ and the LDA-based $\chi(q)$ is better than for $\chi_{\rm KS}(q)$ and $\chi_{\rm RPA}(q)$. From Fig. 13(c), we see that the RPP approximation fails to describe the density response function of the warm dense hydrogen at $r_s = 4$ and $\theta = 1$ with $\Delta \chi(q)$ reaching about 28%. These conclusions are valid for both data sets with $N = 14$ and $N = 20$ particles in the main cell.

In Fig. 14, we show the results for the static XC kernel at $r_s = 4$ and $\theta = 1$. In Fig. 14(a), we present the static XC kernel computed self-consistently from the KS-DFT. In Fig. 14(b), we present the static XC kernel calculated using
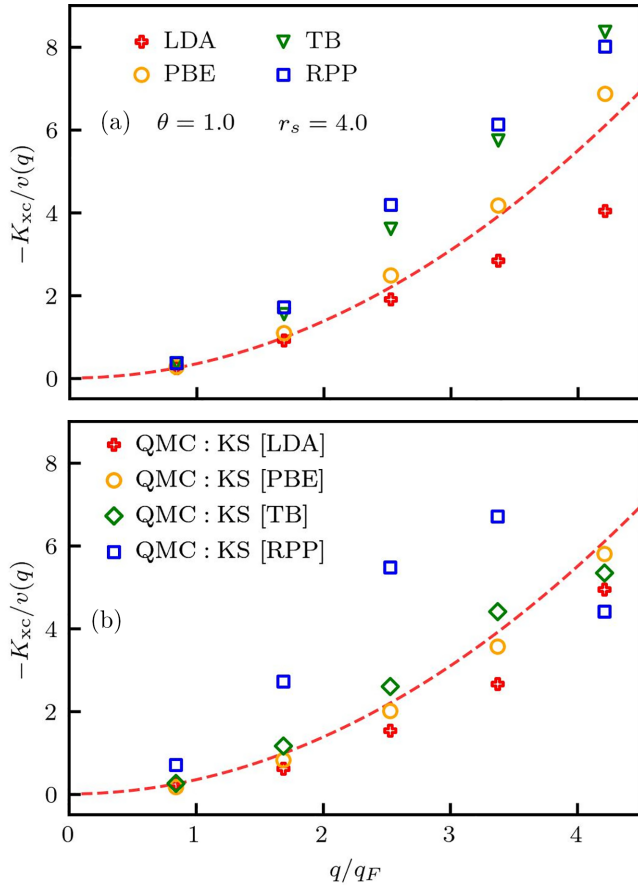
FIG. 14. (a) Fully consistent static XC kernel from KS-DFT simulations with different XC functionals. (b) Static XC-kernel extracted using the PIMC data and KS-response function from KS-DFT simulations. Demonstration of the equivalence of the KS response function from the harmonic perturbation technique and LR-TDDFT calculations. The results are for warm dense hydrogen at $r_s = 4$ and $\theta = 1$.
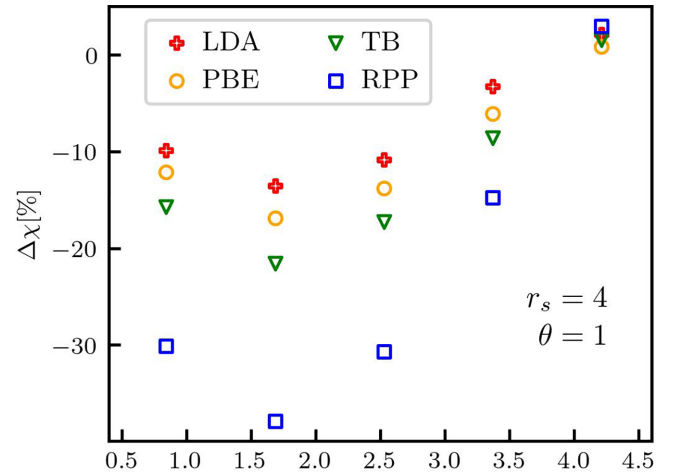

FIG. 15. Inaccuracy in the density response function due to an inconsistent combination of the KS response function and the XC kernel extracted from the PIMC data and an ideal reference function without XC effects. The results are for warm dense hydrogen at $r_s = 4$ and $\theta = 1$.

Let us now consider the performance of the XC kernel computed using the PIMC data for $\chi(q)$ and setting $\chi_{KS}(q) = \chi_{KS}^{NXC}(q)$. As for the case with $r_s = 2$, we use the resulting static XC kernel in Eq. (19) to compute $\chi(q)$. The obtained $\chi(q)$ is compared to the exact PIMC data for $\chi(q)$. The corresponding results are shown in Fig. 15. Comparing relative deviation (error) values presented in Fig. 15 with Fig. 12, we clearly see that the use of the $\chi_{KS}^{NXC}(q)$ as a reference function for the extraction of the XC kernel from the PIMC data for $\chi(q)$ leads to the significantly larger errors for the density response function even compared to the purely KS-DFT based XC kernel. It is clear that a strong localization of electrons around protons invalidates the use of $\chi_{KS}^{NXC}(q)$ as a good reference function.

D. The importance of a consistent KS response function for the static XC kernel

The main goal of the paper is to show how to compute the macroscopic KS response function that can be used together with the $\chi(q)$ for the calculation of the static XC kernel and that can be used for the calculation of $\chi(q, \omega)$ consistently within the *adiabatic approximation*, Eq. (19). The standard way of introducing a macroscopic quantity in the LR-TDDFT at a wave number $\mathbf{q} = \mathbf{k} + \mathbf{G}$ is by setting $\mathbf{G} = \mathbf{G}'$ [42] ($\mathbf{G} = 0$, if $\mathbf{q}$ is in the first Brillouin zone). This is known to be valid for the dielectric function as we also confirm it here independently using the method of direct perturbation. However, setting $\mathbf{G} = \mathbf{G}'$ in a noninteracting density response function $\chi_M^0(q) = \chi_{\mathbf{G},\mathbf{G}}^0(\mathbf{k}, \omega)$ does not give a correct macroscopic KS response function. One of our key findings is that $\chi_{KS}(q, \omega) \neq \chi_M^0(q)$, where $\chi_{KS}(q, \omega)$ is defined by Eq. (18) or, equivalently, by Eq. (13). We have been able to show that Eq. (18) provides a correct macroscopic KS response function by using Eq. (13) within the direct perturbation approach. Now we can demonstrate the effect of an inconsistent $\chi_M^0(q)$ on the extraction of the XC kernel from $\chi(q)$.

the PIMC data for $\chi(q)$. The dashed red line in Fig. 14 represents a quadratic dependence of the LFC $G(q)$ corresponding to the long-wavelength approximation.

From Fig. 14(a), we see that the PBE-based XC kernel is well described by the quadratic curve at $q < 4q_F$. The same is the case for the LDA-based XC kernel at $q \lesssim 2.5q_F$. The TB and RPP-based XC kernels have significantly larger values than the PBE and LDA based data at $q > 2q_F$. All considered XC kernels are in good agreement with each other at $q < q_F$.

In Fig. 14(b), we show the XC kernel computed using the PIMC data for $\chi(q)$. The PIMC XC kernel obtained using the PBE-based $\chi_{KS}(q)$ has values close to the PBE-based XC kernel from KS-DFT. This can be seen by comparing the PBE data positions relative to the dashed red line in Figs. 14(a) and 14(b). This is also the case for the LDA-based data. From Fig. 14(b), we see that at $q > 2q_F$, the PIMC XC kernel computed using the TB-based $\chi_{KS}(q)$ has significant differences compared to the data computed using the LDA- and PBE-based $\chi_{KS}(q)$. The PIMC XC kernel computed using the TB-based $\chi_{KS}(q)$ is in good agreement with the PBE based data at $q < 2q_F$.
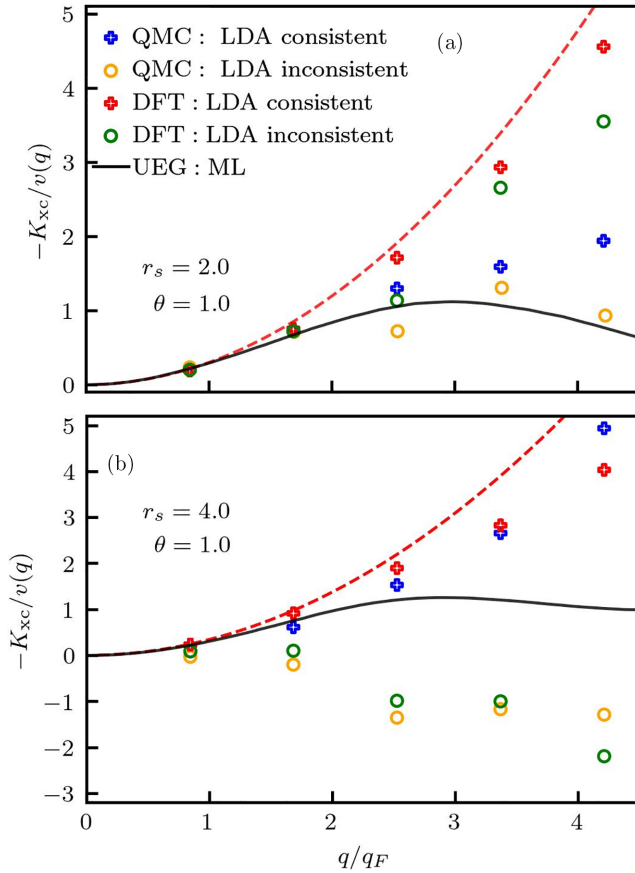
FIG. 16. The XC kernels of warm dense hydrogen computed using consistent and inconsistent KS response functions at (a) $r_s = 2$ and (b) $r_s = 4$ with $\theta = 1$. We also show the exact UEG results based on the neural-net representation of Ref. [75] (solid black line).

In Fig. 16, we compare the static XC kernels extracted from the PIMC and KS-DFT data for $\chi(q)$ using $\chi_{KS}(q)$ (a consistent macroscopic KS response function) and $\chi_M^0(q)$ (an inconsistent macroscopic KS response function). For the KS-DFT data in Fig. 16, we used the LDA functional. From Fig. 16(a), we see that at $r_s = 2$ and $\theta = 1$, the $\chi_{KS}(q)$- and $\chi_M^0(q)$-based data are in agreement with each other at $q < 2q_F$ and significantly differ from each other at $q > 2q_F$. At $r_s = 4$ and $\theta = 1$, we see from Fig. 16(b) that the $\chi_{KS}(q)$- and $\chi_M^0(q)$-based results for the XC kernel differ not only quantitatively, but also qualitatively. Indeed, the $\chi_{KS}(q)$-based XC kernel is always positive, while the XC kernel computed using $\chi_M^0(q)$ has negative values. This qualitative disagreement was interpreted in Ref. [68] as a failure of the adiabatic LDA. Here we show that it is in fact not the failure of the adiabatic LDA, but caused by the use of the $\chi_M^0(q) = \chi_{G,G}^0(\mathbf{k}, \omega)$ as a macroscopic KS response function in Eq. (15).

V. CONCLUSIONS AND OUTLOOK

Recently, with the focus on disordered systems, Moldabekov *et al.* [34] have introduced the direct perturbation-based method for the computation of the static XC kernel for any available XC functional. Here we show how this static XC kernel can be used for the LR-TDDFT calculations of

the dynamic density response function $\chi(q, \omega)$ within the *adiabatic approximation* [represented by Eq. (19) and Fig. 1]. The main point is to use a proper and consistent macroscopic KS response function as introduced by Eq. (18). We reiterate that the presented adiabatic approximation for $\chi(q, \omega)$ has full consistency between the XC functional used for the computation of the XC kernel and for the KS response function. We have demonstrated how the inconsistent combination of the KS response function and XC kernel can lead to quantitatively and even qualitatively wrong results. Additionally, we conclude from the performed analysis that the existence of a universal static XC kernel that works for different parameters is highly unlikely. Instead, one has to use a state and material-specific static XC kernel, which can be computed using the direct perturbation approach.

Furthermore, we have studied in detail the effect of the approximations made to the XC potential on the density response function and XC kernel of warm dense hydrogen. We demonstrated (a) the application of the presented scheme for a static XC kernel that is self-consistent with the reference KS response function, (b) the role of this self-consistency in the description of the static density response function, (c) the analysis of the static density response function using the exact PIMC data for warm dense hydrogen, and (d) the role of the variation in XC functional on the macroscopic KS response function and XC kernel.

We found that at $\theta = 1$, the TR and RPP meta-GGA-level approximations perform worse than the ground-state LDA and PBE functionals. Together with the prior finding of inefficiency of the meta-GGA level SCAN functional at WDM conditions [34], the problems of the TP and RPP for partially degenerate electrons indicate that the standard recipe for the construction of the XC functionals starting on the basis of the LDA does not lead to a better description of WDM. Indeed, even at the LDA level, an explicit inclusion of the temperature dependence into the XC functional leads to a worsening of the KS-DFT result quality at WDM conditions [34]. Therefore, it is clear that XC functional development for the WDM regime requires new innovative approaches. For example, it was recently shown that PBE0-type hybrid-level functionals, mixing exact Hartree-Fock exchange with the PBE exchange, can provide a good description of the UEG at WDM parameters if a mixing coefficient is chosen to reproduce the XC kernel of the UEG [51,52]. Now, using the consistent approach presented in this paper, this analysis of the PBE0-type hybrid-level functional can be extended to real materials like warm dense hydrogen.

An important possible application of the presented consistent adiabatic approximation for $\chi(q, \omega)$ is the analysis and modeling of the XRTS measurements from WDM [106,107]. This is possible since the knowledge of $\chi(q, \omega)$ gives one straightforward access to the dynamic structure factor $S_{ee}(\mathbf{q}, \omega)$ of electrons via the fluctuation-dissipation theorem [47]. Besides, the knowledge of $\chi(q, \omega)$ is equivalent to the knowledge of the dynamical dielectric function $\varepsilon(q, \omega)$, which in turn can be used for the calculation of transport properties like electrical conductivity [32] and stopping power [108].

Finally, we note that a consistent static XC kernel is needed for various other applications such as the construction of effective potentials [47,109–111] for quantum hydrodynamics

[112–116] and plasmonics [117] and the for computation of the energy loss characteristics of high-energy density plasmas [118–120].

[1] A. B. Zylstra, O. A. Hurricane, D. A. Callahan, A. L. Kritcher, J. E. Ralph, H. F. Robey, J. S. Ross, C. V. Young, K. L. Baker, D. T. Casey, T. Döppner, L. Divol, M. Hohenberger, S. L. Pape, A. Pak, P. K. Patel, R. Tommasini, S. J. Ali, P. A. Amendt, L. J. Atherton *et al.*, Burning plasma achieved in inertial fusion, Nature (London) **601**, 542 (2022).

[2] R. Betti and O. A. Hurricane, Inertial-confinement fusion with lasers, Nat. Phys. **12**, 435 (2016).

[3] A. L. Kritcher, D. C. Swift, T. Döppner, B. Bachmann, L. X. Benedict, G. W. Collins, J. L. DuBois, F. Elsner, G. Fontaine, J. A. Gaffney, S. Hamel, A. Lazicki, W. R. Johnson, N. Kostinski, D. Kraus, M. J. MacDonald, B. Maddox, M. E. Martin, P. Neumayer, A. Nikroo *et al.*, A measurement of the equation of state of carbon envelopes of white dwarfs, Nature (London) **584**, 51 (2020).

[4] D. Kraus, J. Vorberger, A. Pak, N. J. Hartley, L. B. Fletcher, S. Frydrych, E. Galtier, E. J. Gamboa, D. O. Gericke, S. H. Glenzer, E. Granados, M. J. MacDonald, A. J. MacKinnon, E. E. McBride, I. Nam, P. Neumayer, M. Roth, A. M. Saunders, A. K. Schuster, P. Sun *et al.*, Formation of diamonds in laser-compressed hydrocarbons at planetary interior conditions, Nat. Astron. **1**, 606 (2017).

[5] A. Lazicki, D. McGonegle, J. R. Rygg, D. G. Braun, D. C. Swift, M. G. Gorman, R. F. Smith, P. G. Heighway, A. Higginbotham, M. J. Suggit, D. E. Fratanduono, F. Coppari, C. E. Wehrenberg, R. G. Kraus, D. Erskine, J. V. Bernier, J. M. McNaney, R. E. Rudd, G. W. Collins, J. H. Eggert *et al.*, Metastability of diamond ramp-compressed to 2 terapascals, Nature (London) **589**, 532 (2021).

[6] D. Kraus, A. Ravasio, M. Gauthier, D. O. Gericke, J. Vorberger, S. Frydrych, J. Helfrich, L. B. Fletcher, G. Schaumann, B. Nagler, B. Barbrel, B. Bachmann, E. J. Gamboa, S. Göde, E. Granados, G. Gregori, H. J. Lee, P. Neumayer, W. Schumaker, T. Döppner *et al.*, Nanosecond formation of diamond and lonsdaleite by shock compression of graphite, Nat. Commun. **7**, 10970 (2016).

[7] A. K. Schuster, K. Voigt, B. Klemmed, N. J. Hartley, J. B. Lütgert, M. zhang, C. Bähtz, A. Benad, C. Brabetz, T. Cowan, T. Doeppner, D. J. Erb, A. Eychmueller, S. Facsko, R. Falcone, L. B. Fletcher, S. Frydrych, G. C. Ganzenmüller, D. O. Gericke, S. H. Glenzer. *et al.*, Recovery of release cloud from laser shock-loaded graphite and hydrocarbon targets: In search of diamonds, J. Phys. D **56**, 025301 (2022).

[8] S. X. Hu, B. Militzer, V. N. Goncharov, and S. Skupsky, First-principles equation-of-state table of deuterium for iner-

tial confinement fusion applications, Phys. Rev. B **84**, 224109 (2011).

[9] T. Tschentscher, C. Bressler, J. Grünert, A. Madsen, A. P. Mancuso, M. Meyer, A. Scherz, H. Sinn, and U. Zastrau, Photon beam transport and scientific instruments at the european XFEL, Appl. Sci. **7**, 592 (2017).

[10] Z. He, M. Rödel, J. Lütgert, A. Bergermann, M. Bethkenhagen, D. Chekrygina, T. E. Cowan, A. Descamps, M. French, E. Galtier, A. E. Gleason, G. D. Glenn, S. H. Glenzer, Y. Inubushi, N. J. Hartley, Jean-Alexis Hernandez, B. Heuser, O. S. Humphries, N. Kamimura, K. Katagiri *et al.*, Diamond formation kinetics in shock-compressed C–H–O samples recorded by small-angle x-ray scattering and x-ray diffraction, Sci. Adv. **8**, eabo0617 (2022).

[11] G. Chabrier, P. Brassard, G. Fontaine, and D. Saumon, Cooling sequences and color-magnitude diagrams for cool white dwarfs with hydrogen atmospheres, Astrophys. J. **543**, 216 (2000).

[12] D. Saumon, W. B. Hubbard, G. Chabrier, and H. M. van Horn, The role of the molecular-metallic transition of hydrogen in the evolution of jupiter, saturn, and brown dwarfs, Astrophys. J. **391**, 827 (1992).

[13] A. K. Schuster, N. J. Hartley, J. Vorberger, T. Döppner, T. van Driel, R. W. Falcone, L. B. Fletcher, S. Frydrych, E. Galtier, E. J. Gamboa, D. O. Gericke, S. H. Glenzer, E. Granados, M. J. MacDonald, A. J. MacKinnon, E. E. McBride, I. Nam, P. Neumayer, A. Pak, I. Prencipe *et al.*, Measurement of diamond nucleation rates from hydrocarbons at conditions comparable to the interiors of icy giant planets, Phys. Rev. B **101**, 054301 (2020).

[14] R. F. Smith, J. H. Eggert, R. Jeanloz, T. S. Duffy, D. G. Braun, J. R. Patterson, R. E. Rudd, J. Biener, A. E. Lazicki, A. V. Hamza, J. Wang, T. Braun, L. X. Benedict, P. M. Celliers, and G. W. Collins, Ramp compression of diamond to five terapascals, Nature (London) **511**, 330 (2014).

[15] J. Daligault and S. Gupta, Electron-ion scattering in dense multi-component plasmas: application to the outer crust of an accreting star, Astrophys. J. **703**, 994 (2009).

[16] *Frontiers and Challenges in Warm Dense Matter*, edited by F. Graziani, M. P. Desjarlais, R. Redmer, and S. B. Trickey (Springer, International Publishing, Switzerland, Cham, 2014).

[17] M. Bonitz, T. Dornheim, Zh. A. Moldabekov, S. Zhang, P. Hamann, H. Kählert, A. Filinov, K. Ramakrishna, and J. Vorberger, *Ab initio* simulation of warm dense matter, Phys. Plasmas **27**, 042710 (2020).

[18] T. Dornheim, Z. A. Moldabekov, K. Ramakrishna, P. Tolias, A. D. Baczewski, D. Kraus, T. R. Preston, D. A. Chapman, M. P. Böhme, T. Döppner, F. Graziani, M. Bonitz, A. Cangi, and J. Vorberger, Electronic density response of warm dense matter, Phys. Plasmas **30**, 032705 (2023).

[19] T. Dornheim, S. Groth, and M. Bonitz, The uniform electron gas at warm dense matter conditions, Phys. Rep. **744**, 1 (2018).

[20] T. Dornheim, Fermion sign problem in path integral Monte Carlo simulations: Quantum dots, ultracold atoms, and warm dense matter, Phys. Rev. E **100**, 023307 (2019).

[21] K. P. Driver and B. Militzer, All-Electron Path Integral Monte Carlo Simulations of Warm Dense Matter: Application to Water and Carbon Plasmas, Phys. Rev. Lett. **108**, 115502 (2012).

[22] A. Pribram-Jones, S. Pittalis, E. K. U. Gross, and K. Burke, Thermal density functional theory in context, in *Frontiers and Challenges in Warm Dense Matter*, edited by F. Graziani, M. P. Desjarlais, R. Redmer, and S. B. Trickey (Springer International Publishing, Cham, 2014), pp. 25–60.

[23] V. V. Karasiev, L. Calderin, and S. B. Trickey, Importance of finite-temperature exchange correlation for warm dense matter calculations, Phys. Rev. E **93**, 063207 (2016).

[24] K. Ramakrishna, T. Dornheim, and J. Vorberger, Influence of finite temperature exchange-correlation effects in hydrogen, Phys. Rev. B **101**, 195129 (2020).

[25] S. H. Glenzer and R. Redmer, X-ray Thomson scattering in high energy density plasmas, Rev. Mod. Phys. **81**, 1625 (2009).

[26] J. Sheffield, D. Froula, S.H. Glenzer, and N.C. Luhmann, *Plasma Scattering of Electromagnetic Radiation: Theory and Measurement Techniques* (Elsevier Science, Amsterdam, 2010).

[27] G. Gregori, S. H. Glenzer, W. Rozmus, R. W. Lee, and O. L. Landen, Theoretical model of x-ray scattering as a dense matter probe, Phys. Rev. E **67**, 026412 (2003).

[28] D. Kraus, B. Bachmann, B. Barbrel, R. W. Falcone, L. B. Fletcher, S. Frydrych, E. J. Gamboa, M. Gauthier, D. O. Gericke, S. H. Glenzer, S. Göde, E. Granados, N. J. Hartley, J. Helfrich, H. J. Lee, B. Nagler, A. Ravasio, W. Schumaker, J. Vorberger, and T. Döppner, Characterizing the ionization potential depression in dense carbon plasmas with high-precision spectrally resolved x-ray scattering, Plasma Phys. Control. Fusion **61**, 014015 (2019).

[29] T. Dornheim, M. Böhme, D. Kraus, T. Döppner, T. R. Preston, Z. A. Moldabekov, and J. Vorberger, Accurate temperature diagnostics for matter under extreme conditions, Nat. Commun. **13**, 7911 (2022).

[30] T. Dornheim, M. P. Böhme, D. A. Chapman, D. Kraus, T. R. Preston, Z. A. Moldabekov, N Schlünzen, A. Cangi, T. Döppner, and J. Vorberger, Imaginary-time correlation function thermometry a new, high-accuracy and model-free temperature analysis technique for x-ray Thomson scattering data, Phys. Plasmas **30**, 042707 (2023).

[31] M.A.L. Marques, N.T. Maitra, F.M.S. Nogueira, E.K.U. Gross, and A. Rubio, *Fundamentals of Time-Dependent Density Functional Theory*, Lecture Notes in Physics (Springer, Berlin, 2012).

[32] P. Hamann, T. Dornheim, J. Vorberger, Z. A. Moldabekov, and M. Bonitz, Dynamic properties of the warm dense electron gas based on *ab initio* path integral Monte Carlo simulations, Phys. Rev. B **102**, 125150 (2020).

[33] E. K. U. Gross and W. Kohn, Local Density-Functional Theory of Frequency-Dependent Linear Response, Phys. Rev. Lett. **55**, 2850 (1985).

[34] Z. Moldabekov, M. Böhme, J. Vorberger, D. Blaschke, and T. Dornheim, *Ab initio* static exchange–correlation kernel across Jacob's ladder without functional derivatives, J. Chem. Theory Comput. **19**, 1286 (2023).

[35] S. Moroni, D. M. Ceperley, and G. Senatore, Static Response from Quantum Monte Carlo Calculations, Phys. Rev. Lett. **69**, 1837 (1992).

[36] S. Moroni, D. M. Ceperley, and G. Senatore, Static Response and Local Field Factor of the Electron Gas, Phys. Rev. Lett. **75**, 689 (1995).

[37] C. Bowen, G. Sugiyama, and B. J. Alder, Static dielectric response of the electron gas, Phys. Rev. B **50**, 14838 (1994).

[38] T. Dornheim, J. Vorberger, and M. Bonitz, Nonlinear Electronic Density Response in Warm Dense Matter, Phys. Rev. Lett. **125**, 085001 (2020).

[39] Z. Moldabekov, J. Vorberger, and T. Dornheim, Density functional theory perspective on the nonlinear response of correlated electrons across temperature regimes, J. Chem. Theory Comput. **18**, 2900 (2022).

[40] N. Wiser, Dielectric constant with local field effects included, Phys. Rev. **129**, 62 (1963).

[41] S. L. Adler, Quantum theory of the dielectric constant in real solids, Phys. Rev. **126**, 413 (1962).

[42] C. A. Ullrich, *Time-Dependent Density-Functional Theory: Concepts and Applications* (Oxford University Press, Oxford, 2011).

[43] A. A. Kugler, Theory of the local field correction in an electron gas, J. Stat. Phys. **12**, 35 (1975).

[44] C. Fortmann, A. Wierling, and G. Röpke, Influence of local-field corrections on Thomson scattering in collision-dominated two-component plasmas, Phys. Rev. E **81**, 026405 (2010).

[45] H. Reinholz, R. Redmer, G. Röpke, and A. Wierling, Long-wavelength limit of the dynamical local-field factor and dynamical conductivity of a two-component plasma, Phys. Rev. E **62**, 5648 (2000).

[46] P. Hamann, J. Vorberger, T. Dornheim, Z. A. Moldabekov, and M. Bonitz, Ab initio results for the plasmon dispersion and damping of the warm dense electron gas, Contrib. Plasma Phys. **60**, e202000147 (2020).

[47] G. Giuliani and G. Vignale, *Quantum Theory of the Electron Liquid* (Cambridge University Press, Cambridge, 2008).

[48] K. Kunc and E. Tosatti, "direct" evaluation of the inverse dielectric matrix in semiconductors, Phys. Rev. B **29**, 7045 (1984).

[49] A. Fleszar and R. Resta, Dielectric matrices in semiconductors: A direct approach, Phys. Rev. B **31**, 5305 (1985).

[50] A. Sakko, A. Rubio, M. Hakala, and K. Hämäläinen, Time-dependent density functional approach for the calculation of inelastic x-ray scattering spectra of molecules, J. Chem. Phys. **133**, 174111 (2010).

[51] Z. Moldabekov, M. Lokamani, J. Vorberger, A. Cangi, and T. Dornheim, Assessing the accuracy of hybrid exchange-correlation functionals for the density response of warm dense electrons, J. Chem. Phys. **158**, 094105 (2023).

[52] Z. A. Moldabekov, M. Lokamani, J. Vorberger, A. Cangi, and T. Dornheim, Non-empirical mixing coefficient for hybrid XC functionals from analysis of the XC kernel, J. Phys. Chem. Lett. **14**, 1326 (2023).

[53] A. D. Baczewski, L. Shulenburger, M. P. Desjarlais, S. B. Hansen, and R. J. Magyar, X-ray Thomson Scattering in Warm Dense Matter Without the Chihara Decomposition, Phys. Rev. Lett. **116**, 115004 (2016).

[54] K. Ramakrishna, M. Lokamani, A. Baczewski, J. Vorberger, and A. Cangi, Electrical conductivity of iron in earth's core from microscopic Ohm's law, Phys. Rev. B **107**, 115131 (2023).

[55] Young-Moo Byun, J. Sun, and Carsten A Ullrich, Time-dependent density-functional theory for periodic solids: Assessment of excitonic exchange–correlation kernels, Electron. Struct. **2**, 023002 (2020).

[56] G. Adragna, R. Del Sole, and A. Marini, *Ab initio* calculation of the exchange-correlation kernel in extended systems, Phys. Rev. B **68**, 165108 (2003).

[57] R. M. Martin, L. Reining, and D. M. Ceperley, *Interacting Electrons: Theory and Computational Approaches* (Cambridge University Press, Cambridge, 2016).

[58] M. S. Hybertsen and S. G. Louie, *Ab initio* static dielectric matrices from the density-functional approach. I. Formulation and application to semiconductors and insulators, Phys. Rev. B **35**, 5585 (1987).

[59] G. Onida, L. Reining, and A. Rubio, Electronic excitations: Density-functional versus many-body Green's-function approaches, Rev. Mod. Phys. **74**, 601 (2002).

[60] I. G. Gurtubay, J. M. Pitarke, W. Ku, A. G. Eguiluz, B. C. Larson, J. Tischler, P. Zschack, and K. D. Finkelstein, Electron-hole and plasmon excitations in 3*d* transition metals: *Ab initio* calculations and inelastic x-ray scattering measurements, Phys. Rev. B **72**, 125117 (2005).

[61] S. Ichimaru, S. Mitake, S. Tanaka, and Xin-Zhong Yan, Theory of interparticle correlations in dense, high-temperature plasmas. I. General formalism, Phys. Rev. A **32**, 1768 (1985).

[62] P. Hollebon, O. Ciricosta, M. P. Desjarlais, C. Cacho, C. Spindloe, E. Springate, I. C. E. Turcu, J. S. Wark, and S. M. Vinko, *Ab initio* simulations and measurements of the free-free opacity in aluminum, Phys. Rev. E **100**, 043207 (2019).

[63] S. Ichimaru, Strongly coupled plasmas: High-density classical plasmas and degenerate electron liquids, Rev. Mod. Phys. **54**, 1017 (1982).

[64] P. Sperling, E. J. Gamboa, H. J. Lee, H. K. Chung, E. Galtier, Y. Omarbakiyeva, H. Reinholz, G. Röpke, U. Zastrau, J. Hastings, L. B. Fletcher, and S. H. Glenzer, Free-Electron X-ray Laser Measurements of Collisional-Damped Plasmons in Isochorically Heated Warm Dense Matter, Phys. Rev. Lett. **115**, 115001 (2015).

[65] B. B. L. Witte, L. B. Fletcher, E. Galtier, E. Gamboa, H. J. Lee, U. Zastrau, R. Redmer, S. H. Glenzer, and P. Sperling, Warm Dense Matter Demonstrating Non-Drude Conductivity from Observations of Nonlinear Plasmon Damping, Phys. Rev. Lett. **118**, 225001 (2017).

[66] K. Plagemann, P. Sperling, R. Thiele, M. Desjarlais, C. Fortmann, T. Döppner, H. Lee, Siegfried H Glenzer, and R. Redmer, Dynamic structure factor in warm dense beryllium, New J. Phys. **14**, 055020 (2012).

[67] D. Kremp, M. Schlanges, and T. Bornath, *Quantum Statistics of Nonideal Plasmas*, Springer Series on Atomic, Optical, and Plasma Physics (Springer, Switzerland, Cham, 2005).

[68] M. Böhme, Z. A. Moldabekov, J. Vorberger, and T. Dornheim, Static Electronic Density Response of Warm Dense Hydrogen: *Ab initio* Path Integral Monte Carlo Simulations, Phys. Rev. Lett. **129**, 066402 (2022).

[69] T. Dornheim, M. Böhme, Z. A. Moldabekov, J. Vorberger, and M. Bonitz, Density response of the warm dense electron gas beyond linear response theory: Excitation of harmonics, Phys. Rev. Res. **3**, 033231 (2021).

[70] J. P. Perdew and K. Schmidt, Jacob's ladder of density functional approximations for the exchange-correlation energy, AIP Conf. Proc. **577**, 1 (2001).

[71] J. Tao, J. P. Perdew, V. N. Staroverov, and G. E. Scuseria, Climbing the Density Functional Ladder: Nonempirical Meta-Generalized Gradient Approximation Designed for Molecules and Solids, Phys. Rev. Lett. **91**, 146401 (2003).

[72] T. Dornheim, S. Groth, J. Vorberger, and M. Bonitz, *Ab initio* Path Integral Monte Carlo Results for the Dynamic Structure Factor of Correlated Electrons: From the Electron Liquid to Warm Dense Matter, Phys. Rev. Lett. **121**, 255001 (2018).

[73] Zh.A. Moldabekov, S. Groth, T. Dornheim, H. Kählert, M. Bonitz, and T. S. Ramazanov, Structural characteristics of strongly coupled ions in a dense quantum plasma, Phys. Rev. E **98**, 023207 (2018).

[74] Z. Moldabekov, P. Ludwig, M. Bonitz, and T. Ramazanov, Ion potential in warm dense matter: Wake effects due to streaming degenerate electrons, Phys. Rev. E **91**, 023102 (2015).

[75] T. Dornheim, J. Vorberger, S. Groth, N. Hoffmann, Zh. A. Moldabekov, and M. Bonitz, The static local field correction of the warm dense electron gas: An *ab initio* path integral Monte Carlo study and machine learning representation, J. Chem. Phys. **151**, 194104 (2019).

[76] T. Dornheim, Zhandos A. Moldabekov, J. Vorberger, and S. Groth, *Ab initio* path integral Monte Carlo simulation of the uniform electron gas in the high energy density regime, Plasma Phys. Controlled Fusion **62**, 075003 (2020).

[77] Z. Moldabekov, T. Dornheim, M. Böhme, J. Vorberger, and A. Cangi, The relevance of electronic perturbations in the warm dense electron gas, J. Chem. Phys. **155**, 124116 (2021).

[78] Z. A. Moldabekov, T. Dornheim, and A. Cangi, Thermal excitation signals in the inhomogeneous warm dense electron gas, Sci. Rep. **12**, 1093 (2022).

[79] X. Gonze, B. Amadon, G. Antonius, F. Arnardi, L. Baguet, J.-M. Beuken, J. Bieder, F. Bottin, J. Bouchet, E. Bousquet, N. Brouwer, F. Bruneval, G. Brunin, Théo Cavignac, J.-B. Charraud, W. Chen, M. Côté, S. Cottenier, J. Denier, Grégory Geneste *et al.*, The ABINIT project: Impact, environment and recent developments, Comput. Phys. Commun. **248**, 107042 (2020).

[80] A. H. Romero, D. C. Allan, B. Amadon, G. Antonius, T. Applencourt, L. Baguet, J. Bieder, F. Bottin, J. Bouchet, E. Bousquet, F. Bruneval, G. Brunin, D. Caliste, M. Côté, J. Denier, C. Dreyer, P. Ghosez, M. Giantomassi, Y. Gillet, O. Gingras *et al.*, ABINIT: Overview, and focus on selected capabilities, J. Chem. Phys. **152**, 124102 (2020).

[81] X. Gonze, F. Jollet, F. Abreu Araujo, D. Adams, B. Amadon, T. Applencourt, C. Audouze, J.-M. Beuken, J. Bieder, A.

Bokhanchuk, E. Bousquet, F. Bruneval, D. Caliste, M. Côté, F. Dahm, F. Da Pieve, M. Delaveau, M. Di Gennaro, B. Dorado, C. Espejo *et al.*, Recent developments in the ABINIT software package, Comput. Phys. Commun. **205**, 106 (2016).

[82] X. Gonze, B. Amadon, P.-M. Anglade, J.-M. Beuken, F. Bottin, P. Boulanger, F. Bruneval, D. Caliste, R. Caracas, M. Côté, T. Deutsch, L. Genovese, Ph. Ghosez, M. Giantomassi, S. Goedecker, D.R. Hamann, P. Hermet, F. Jollet, G. Jomard, S. Leroux *et al.*, ABINIT: First-principles approach to material and nanosystem properties, Comput. Phys. Commun. **180**, 2582 (2009).

[83] X. Gonze, G.-M. Rignanese, M. Verstraete, J.-M. Beuken, Y. Pouillon, R. Caracas, F. Jollet, M. Torrent, G. Zerah, M. Mikami, Ph. Ghosez, M. Veithen, J.-Y. Raty, V. Olevano, F. Bruneval, L. Reining, R. Godby, G. Onida, and D.R. Hamann D.C. Allan, A brief introduction to the ABINIT software package, Z. Kristallog. Crystal. Mater. **220**, 558 (2005).

[84] X. Gonze, J.-M. Beuken, R. Caracas, F. Detraux, M. Fuchs, G.-M. Rignanese, L. Sindic, M. Verstraete, G. Zerah, F. Jollet, M. Torrent, A. Roy, M. Mikami, Ph. Ghosez, J.-Y. Raty, and D.C. Allan, First-principles computation of material properties: The ABINIT software project, Comput. Mater. Sci. **25**, 478 (2002).

[85] S. Goedecker, M. Teter, and J. Hutter, Separable dual-space Gaussian pseudopotentials, Phys. Rev. B **54**, 1703 (1996).

[86] J. P. Perdew and A. Zunger, Self-interaction correction to density-functional approximations for many-electron systems, Phys. Rev. B **23**, 5048 (1981).

[87] J. J. Mortensen, L. B. Hansen, and K. W. Jacobsen, Real-space grid implementation of the projector augmented wave method, Phys. Rev. B **71**, 035109 (2005).

[88] J. Enkovaara, C. Rostgaard, J. J. Mortensen, J. Chen, M. Dułak, L. Ferrighi, J. Gavnholt, C. Glinsvad, V. Haikola, H. A. Hansen, H. H. Kristoffersen, M. Kuisma, A. H. Larsen, L. Lehtovaara, M. Ljungberg, O. Lopez-Acevedo, P. G. Moses, J. Ojanen, T. Olsen, V. Petzold *et al.*, Electronic structure calculations with GPAW: A real-space implementation of the projector augmented-wave method, J. Phys.: Condens. Matter **22**, 253202 (2010).

[89] A. H. Larsen, J. J. Mortensen, J. Blomqvist, I. E. Castelli, R. Christensen, M. Dułak, J. Friis, M. N. Groves, B. Hammer, C. Hargus, E. D. Hermes, P. C. Jennings, P. B. Jensen, J. Kermode, J. R. Kitchin, E. L. Kolsbjerg, J. Kubal, K. Kaasbjerg, S. Lysgaard, J. B. Maronsson *et al.*, The atomic simulation environment—a Python library for working with atoms, J. Phys.: Condens. Matter **29**, 273002 (2017).

[90] S. R. Bahn and K. W. Jacobsen, An object-oriented scripting interface to a legacy electronic structure code, Comput. Sci. Eng. **4**, 56 (2002).

[91] J. Yan, J. J. Mortensen, K. W. Jacobsen, and K. S. Thygesen, Linear density response function in the projector augmented wave method: Applications to solids, surfaces, and interfaces, Phys. Rev. B **83**, 245122 (2011).

[92] L. Fiedler, Z. A. Moldabekov, X. Shao, K. Jiang, T. Dornheim, M. Pavanello, and A. Cangi, Accelerating equilibration in first-principles molecular dynamics with orbital-free density functional theory, Phys. Rev. Res. **4**, 043033 (2022).

[93] J. P. Perdew and Y. Wang, Accurate and simple analytic representation of the electron-gas correlation energy, Phys. Rev. B **45**, 13244 (1992).

[94] M. Böhme, Z. A. Moldabekov, J. Vorberger, and T. Dornheim, Ab initio path integral Monte Carlo simulations of hydrogen snapshots at warm dense matter conditions, Phys. Rev. E **107**, 015206 (2023).

[95] A. J. Cohen, P. Mori-Sánchez, and W. Yang, Insights into current limitations of density functional theory, Science **321**, 792 (2008).

[96] A. Kokalj, Xcrysden'a new program for displaying crystalline structures and electron densities, J. Mol. Graphics Modell. **17**, 176 (1999).

[97] A. Kokalj, Computer graphics and graphical user interfaces as tools in simulations of matter at the atomic scale, Comput. Mater. Sci. **28**, 155 (2003), Proceedings of the Symposium on Software Development for Process and Materials Design.

[98] J. P. Perdew, K. Burke, and M. Ernzerhof, Generalized Gradient Approximation Made Simple, Phys. Rev. Lett. **77**, 3865 (1996).

[99] J. P. Perdew, A. Ruzsinszky, G. I. Csonka, O. A. Vydrov, G. E. Scuseria, L. A. Constantin, X. Zhou, and K. Burke, Restoring the Density-Gradient Expansion for Exchange in Solids and Surfaces, Phys. Rev. Lett. **100**, 136406 (2008).

[100] R. Armiento and A. E. Mattsson, Functional designed to include surface effects in self-consistent density functional theory, Phys. Rev. B **72**, 085108 (2005).

[101] J. Sun, A. Ruzsinszky, and J. P. Perdew, Strongly Constrained and Appropriately Normed Semilocal Density Functional, Phys. Rev. Lett. **115**, 036402 (2015).

[102] S. Groth, T. Dornheim, T. Sjostrom, F. D. Malone, W. M. C. Foulkes, and M. Bonitz, *Ab initio* Exchange–Correlation Free Energy of the Uniform Electron Gas at Warm Dense Matter Conditions, Phys. Rev. Lett. **119**, 135001 (2017).

[103] F. Tran and P. Blaha, Accurate Band Gaps of Semiconductors and Insulators With a Semilocal Exchange-Correlation Potential, Phys. Rev. Lett. **102**, 226401 (2009).

[104] E. Räsänen, S. Pittalis, and C. R. Proetto, Universal correction for the Becke–Johnson exchange potential, J. Chem. Phys. **132**, 044112 (2010).

[105] A. D. Becke and E. R. Johnson, A simple effective potential for exchange, J. Chem. Phys. **124**, 221101 (2006).

[106] T. R. Preston, K. Appel, E. Brambrink, B. Chen, L. B. Fletcher, C. Fortmann-Grote, S. H. Glenzer, E. Granados, S. Göde, Z. Konôpková, H. J. Lee, H. Marquardt, E. E. McBride, B. Nagler, M. Nakatsutsumi, P. Sperling, B. B. L. Witte, and U. Zastrau, Measurements of the momentum-dependence of plasmonic excitations in matter around 1 mbar using an x-ray free electron laser, Appl. Phys. Lett. **114**, 014101 (2019).

[107] S. H. Glenzer, L. B. Fletcher, E. Galtier, B. Nagler, R. Alonso-Mori, B. Barbrel, S. B. Brown, D. A. Chapman, Z. Chen, C. B. Curry, F. Fiuza, E. Gamboa, M. Gauthier, D. O. Gericke, A. Gleason, S. Goede, E. Granados, P. Heimann, J. Kim, D. Kraus *et al.*, Matter under extreme conditions experiments at the Linac Coherent Light Source, J. Phys. B: At. Mol. Opt. Phys. **49**, 092001 (2016).

[108] Zh. A. Moldabekov, T. Dornheim, M. Bonitz, and T. S. Ramazanov, Ion energy-loss characteristics and friction in a free-electron gas at warm dense matter and nonideal dense plasma conditions, Phys. Rev. E **101**, 053203 (2020).

[109] T. Dornheim, P. Tolias, Z. A. Moldabekov, A. Cangi, and J. Vorberger, Effective electronic forces and potentials from

ab initio path integral Monte Carlo simulations, J. Chem. Phys. **156**, 244113 (2022).

[110] G. Senatore, S. Moroni, and D. M. Ceperley, Local field factor and effective potentials in liquid metals, J. Non-Cryst. Solids **205-207**, 851 (1996).

[111] Zh. A. Moldabekov, H. Kählert, T. Dornheim, S. Groth, M. Bonitz, and T. S. Ramazanov, Dynamical structure factor of strongly coupled ions in a dense quantum plasma, Phys. Rev. E **99**, 053203 (2019).

[112] A. Diaw and M.S. Murillo, A viscous quantum hydrodynamics model based on dynamic density functional theory, Sci. Rep. **7**, 15352 (2017).

[113] Zh. A. Moldabekov, M. Bonitz, and T. S. Ramazanov, Theoretical foundations of quantum hydrodynamics for plasmas, Phys. Plasmas **25**, 031903 (2018).

[114] Z. A. Moldabekov, T. Dornheim, G. Gregori, F. Graziani, M. Bonitz, and A. Cangi, Towards a quantum fluid theory of correlated many-fermion systems from first principles, SciPost Phys. **12**, 062 (2022).

[115] F. Graziani, Z. Moldabekov, B. Olson, and M. Bonitz, Shock physics in warm dense matter: A quantum hydrody-

namics perspective, Contrib. Plasma Phys. **62**, e202100170 (2022).

[116] Zh. A. Moldabekov, M. Bonitz, and T.S. Ramazanov, Gradient correction and bohm potential for two- and one-dimensional electron gases at a finite temperature, Contrib. Plasma Phys. **57**, 499 (2017).

[117] F. Della Sala, Orbital-free methods for plasmonics: Linear response, J. Chem. Phys. **157**, 104101 (2022).

[118] R. J. Cortez and J. T. Cassibry, Stopping power in d6li plasmas for target ignition studies, Nucl. Fusion **58**, 026009 (2018).

[119] M. K. Issanova, S. K. Kodanova, T. S. Ramazanov, N. Kh. Bastykova, Zh. A. Moldabekov, and C.-V. Meister, Classical scattering and stopping power in dense plasmas: The effect of diffraction and dynamic screening, Laser Part. Beams **34**, 457 (2016).

[120] Y. H. Ding, A. J. White, S. X. Hu, O. Certik, and L. A. Collins, *Ab initio* Studies on the Stopping Power of Warm Dense Matter with Time-Dependent Orbital-Free Density Functional Theory, Phys. Rev. Lett. **121**, 145001 (2018).